Article

Cell Reports

Cellular Classes in the Human Brain Revealed *In Vivo* by Heartbeat-Related Modulation of the Extracellular Action Potential Waveform

Graphical Abstract

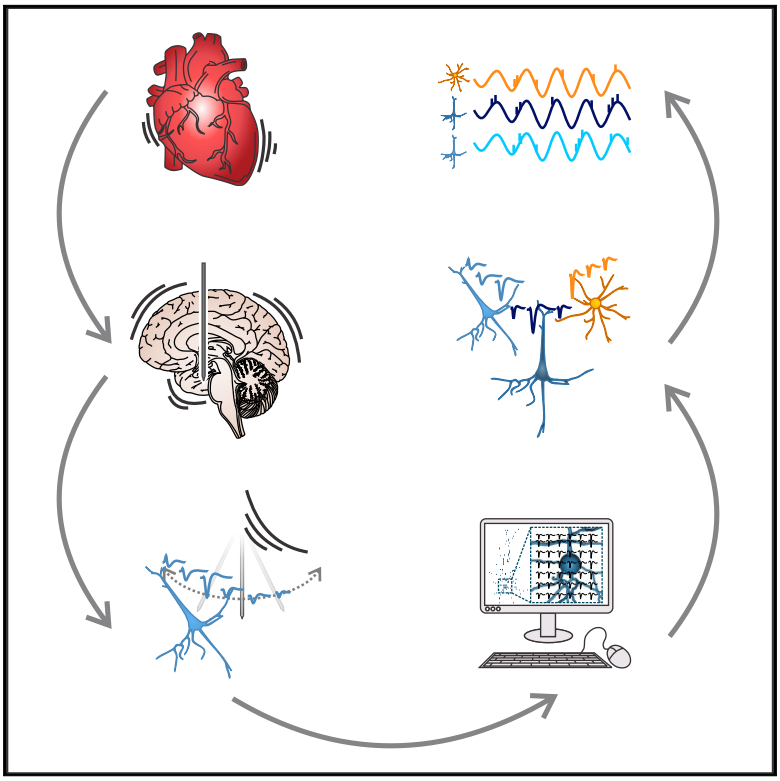

Authors

Clayton P. Mosher, Yina Wei, Jan Kamiński, Anirban Nandi, Adam N. Mamelak, Costas A. Anastassiou, Ueli Rutishauser

Correspondence

costasa@alleninstitute.org (C.A.A.), ueli.rutishauser@cshs.org (U.R.)

In Brief

During the heartbeat, the brain pulsates and recording electrodes move. Mosher et al. show that, in the living human brain, such movement affects the spike waveform leading to enhanced separation between cell types. Single-cell models of human neurons reveal distinct properties of the cell types identified *in vivo*.

Highlights

- When the heart beats, recording electrodes inside the human brain move
- Movement elicits features of the action potential that improve cell typing *in vivo*
- Human single-cell modeling infers cellular properties of identified cell types
- Newly detected cell types exhibit differential coupling to local oscillations

Mosher et al., 2020, Cell Reports *30*, 3536–3551
March 10, 2020
https://doi.org/10.1016/j.celrep.2020.02.027

CellPress

OPEN ACCESS
CellPress

Cell Reports
Article

Cellular Classes in the Human Brain Revealed *In Vivo* by Heartbeat-Related Modulation of the Extracellular Action Potential Waveform

Clayton P. Mosher,[1,7] Yina Wei,[2,7] Jan Kamiński,[1,6] Anirban Nandi,[2] Adam N. Mamelak,[1] Costas A. Anastassiou,[2,3,8,*] and Ueli Rutishauser[1,4,5,6,8,9,*]

[1]Department of Neurosurgery, Cedars-Sinai Medical Center, Los Angeles, CA 90048, USA
[2]Allen Institute for Brain Science, Seattle, WA 98109, USA
[3]Division of Neurology, University of British Columbia, Vancouver, BC V6T 1Z4, Canada
[4]Center for Neural Science and Medicine, Cedars-Sinai Medical Center, Los Angeles, CA 90048, USA
[5]Department of Neurology, Cedars-Sinai Medical Center, Los Angeles, CA 90048, USA
[6]Division of Biology and Biological Engineering, Caltech, Pasadena, CA 91125, USA
[7]These authors contributed equally
[8]These authors contributed equally
[9]Lead Contact
*Correspondence: costasa@alleninstitute.org (C.A.A.), ueli.rutishauser@cshs.org (U.R.)
https://doi.org/10.1016/j.celrep.2020.02.027

SUMMARY

Determining cell types is critical for understanding neural circuits but remains elusive in the living human brain. Current approaches discriminate units into putative cell classes using features of the extracellular action potential (EAP); in absence of ground truth data, this remains a problematic procedure. We find that EAPs in deep structures of the brain exhibit robust and systematic variability during the cardiac cycle. These cardiac-related features refine neural classification. We use these features to link bio-realistic models generated from *in vitro* human whole-cell recordings of morphologically classified neurons to *in vivo* recordings. We differentiate aspiny inhibitory and spiny excitatory human hippocampal neurons and, in a second stage, demonstrate that cardiac-motion features reveal two types of spiny neurons with distinct intrinsic electrophysiological properties and phase-locking characteristics to endogenous oscillations. This multi-modal approach markedly improves cell classification in humans, offers interpretable cell classes, and is applicable to other brain areas and species.

INTRODUCTION

Complex behaviors depend on the recruitment and cooperation of many types of excitatory and inhibitory cells within and across brain circuits (Buzsáki, 2006; Klausberger and Somogyi, 2008). Advances in genetic sequencing offer an increasing ability to identify and separate between cell types, giving rise to a more elaborate view of the composition of brain circuits (e.g., Hodge et al., 2018; Soltesz and Losonczy, 2018; Tasic et al., 2018). How these cell types contribute to high-level functions *in vivo* remains largely unknown. This is particularly true in humans, where little is known about how genetically distinct neural classes differ in their electrophysiological or morphological properties, how they behave *in vivo*, and how they support cognition (Anastassiou and Shai, 2016; Buzsáki et al., 2012). The primary means of monitoring the activity of brain circuits *in vivo* are extracellular recordings where putative excitatory and inhibitory cells are identified based on features of the extracellular action potential (EAP) waveform (Buzsáki, 2004; Buzsáki and Draguhn, 2004). More recently, genetic markers and fluorescence imaging have been used to monitor specific types of neurons in rodents (Kohara et al., 2014; Senzai and Buzsáki, 2017) and monkeys (Stauffer et al., 2016). Such cell-type-specific resolution is lacking in humans because genetic manipulation *in vivo* remains infeasible.

In humans and nonhuman primates, the classification of putative inhibitory interneurons and excitatory pyramidal cells is often based on the width of the EAP waveform. Units with broad spiking (BS) waveforms are classified as pyramidal cells, while units with narrow spiking (NS) waveforms are classified as interneurons (Barthó et al., 2004; Connors and Gutnick, 1990; Markram et al., 2004; McCormick et al., 1985; Peyrache et al., 2012; Rao et al., 1999; Sirota et al., 2008; Wilson, 1994). NS and BS waveforms have been directly linked to these two classes in some instances using intra- or juxtacellular monitoring in rodents and monkeys (González-Burgos et al., 2019; Joshi and Hawken, 2006; Krimer et al., 2005; McCormick et al., 1985), cross-correlation of spike trains to reveal monosynaptic excitatory and inhibitory connections (Barthó et al., 2004; Mendoza et al., 2016; Peyrache et al., 2012; Tamura et al., 2004), and antidromic electrical stimulation to identify excitatory projection neurons (Johnston et al., 2009). Importantly, *in vivo* recordings throughout the brain reveal that groups of neurons with NS or BS EAPs play functionally distinct roles in behavior (Anastassiou et al., 2015; Ison et al., 2011; Mitchell et al., 2007; Oemisch et al., 2015; Peyrache et al., 2012; Peyrache and Destexhe, 2019; Rutishauser et al., 2015; Takahashi et al., 2015; Trainito et al., 2019; Viskontas

et al., 2007). Nevertheless, the assumption that all NS cells are inhibitory and all BS cells are excitatory is not always true: some excitatory cells elicit narrow spikes and some inhibitory cells elicit wider spikes (Freund and Buzsáki, 1996; Gray and McCormick, 1996; Onorato et al., 2020; Vigneswaran et al., 2011 Gouwens et al., 2019). Apart from the procedures outlined above (which are often impractical or impossible to perform in human recordings), we lack a method for relating EAPs to the spectrum of cell types identified and predicted by genetics, morphology, and electrophysiology in humans and in monkeys. While several studies have identified EAP clusters beyond NS and BS types in primates and have demonstrated distinct functional roles for these different classes (Ardid et al., 2015; Onorato et al., 2020; Trainito et al., 2019), as yet we are unable to link these putative cell classes to the cell types recognized based on slice electrophysiology and predicted by genetics.

One reason it is difficult to assign cellular identity using features of the average EAP is that the EAP does not directly reflect the intracellular action potential waveform (Anastassiou et al., 2015). In fact, the EAP waveform reflects details of the recording electrode (dimension, material; Nelson and Pouget, 2012), properties of the extracellular space (distance to neuron, conductance Logothetis et al., 2007; Anastassiou et al., 2015), the cellular morphology (e.g., Gold et al., 2006; Hunt et al., 2019), the ionic composition of the cell, and other aspects such as brain state (Buzsáki et al., 1996). As the recording electrode moves farther away from the cell body of a neuron, the EAP width increases (Gold et al., 2007), so that the same neuron, recorded at different distances, can appear to elicit a range of narrow and broad EAP widths (Pettersen and Einevoll, 2008). By considering how the EAP varies at multiple locations around a cell with high-density electrodes in rodents, cell types beyond the NS versus BS distinction can be identified in the awake behaving animal (Jia et al., 2019). In the human brain, there is a disconnect between the number of morphological and genetically distinct neural subtypes (Aevermann et al., 2018; DeFelipe et al., 2013; Hodge et al., 2018) (the adult rodent neocortex is estimated to consist of more than 100; Tasic et al., 2018), and the types we are able to differentiate *in vivo* based on distinctive EAP properties. Moreover, it has been inherently difficult to interpret distinguishing EAP properties (beyond width) and link them to known intracellular features of neural types.

In many experimental paradigms, especially in humans with chronic implants, recordings are restricted to electrodes for which the activity of a neuron is detectable only on a single channel (e.g., on a microwire or a single shank of the Utah array). To improve the spatial sampling using only a single channel, one option in acute paradigms is to drive the electrode in small steps and record from the same neuron at several locations. Another possibility in both acute and chronic recordings is to take advantage of the motion produced through inherent physiological mechanisms, e.g., pulsatile motion of the brain caused by rhythmic changes in intracranial pressure during the heartbeat. While typically perceived as an unwanted effect that compromises data collection (Chen et al., 2012; Fee, 2000; Srivastava et al., 2005), here we propose that periodic, heartbeat-related motion improves the spatial sampling of the extracellular space. Just as high-density recordings improve unit classification compared to microwire recordings, this periodic sampling offers insights into the spatiotemporal variability of EAP features, which, in turn, can be linked to distinct, cell-class-dependent properties.

RESULTS

The EAP Waveform Is Modulated by Cardiac Motion

During the heartbeat, the intracranial pressure changes. We hypothesize that this causes electrodes to move (Figure 1A). If an electrode moves during a cardiac pressure wave, then the EAP will be recorded at different locations around a cell (Figure 1B). In this study, we monitored the heartbeat (electrocardiogram [EKG]) and isolated 1,090 single units from 31 awake behaving humans across 47 recording sessions. We recorded neurons from both subcortical (hippocampus [HIPP], amygdala [AMY], putamen [PUT], substantia nigra [SN], subthalamic nucleus [STN]) and cortical structures (orbitofrontal cortex [OFC], anterior cingulate cortex [ACC], pre-supplementary motor area [pre-SMA]) (Figures 1C and S1A; Tables S1 and S2).

We quantified four features of the EAP waveform: amplitude (AMP), half-width (HW), trough-to-peak width (TPW), and repolarization time (REP; Figure 1D). We calculated these "standard" EAP features for the mean EAP of each unit. We also aligned the single-unit spike times to the R-wave of the EKG, i.e., the prominent peak that denotes ventricular depolarization and muscular contraction that initiates the cardiac cycle. Through spike-R-wave alignment, we observed that EAP features of the same unit varied consistently and periodically as a function of the cardiac cycle (Figure 1E). For example, some units exhibited an increase in EAP AMP toward the end of the cardiac cycle with a concomitant decrease in EAP HW (Figure 1E, left panel) while others exhibited the inverse response (Figure 1E, middle panel)

To quantify the periodic variation of each feature during the cardiac cycle, we calculated a motion index (MI, see STAR Methods, e.g., an MI = 5.0 indicates that the feature increases by 5% during the cardiac cycle). On average, the EAP AMP varied 1.7% +/- 0.78% throughout the brain, with the strongest modulations in deep-brain structures (Figure 1F, AMP MI of deep subcortical structures: AMY = 2.6, HIPP = 2.3, PUT = 1.7, SN = 1.9, STN = 2.7 versus cortex: ACC = 0.9, OFC = 0.88, pre-SMA = 0.8). Across all neurons recorded in a brain area, the EAP was significantly modulated by the cardiac cycle in HIPP, AMY, PUT, STN, and SN ($p = 1.9 \times 10^{-12}$, 0, 0.031, 0.025, 0.0003) but not in ACC, OFC, or pre-SMA (p = 0.147, 0.269, 0.115). The average AMP MI in subcortical structures was significantly higher than in cortex, suggesting that brain motion associated with the cardiac R-wave is stronger in deep-brain structures (subcortical = 2.24 +/- 0.44, cortex = 0.87 +/- 0.04; t test, t(6) = 5.189, p = 0.002).

EAP features covary with distance from the recording electrode, e.g., with increasing distance between electrode and cell body, dendritic currents give rise to an increase in EAP HW as the AMP decreases (Anastassiou et al., 2015; Gold et al., 2006; Pettersen and Einevoll, 2008). We captured these dependencies by calculating a motion correlation (MC) metric between each EAP feature and AMP (see STAR Methods). This metric shows, for example, that AMP and HW were often anticorrelated with an MC of -0.15 ± 0.45 HW/AMP across all cells (mean ± SD); i.e.,

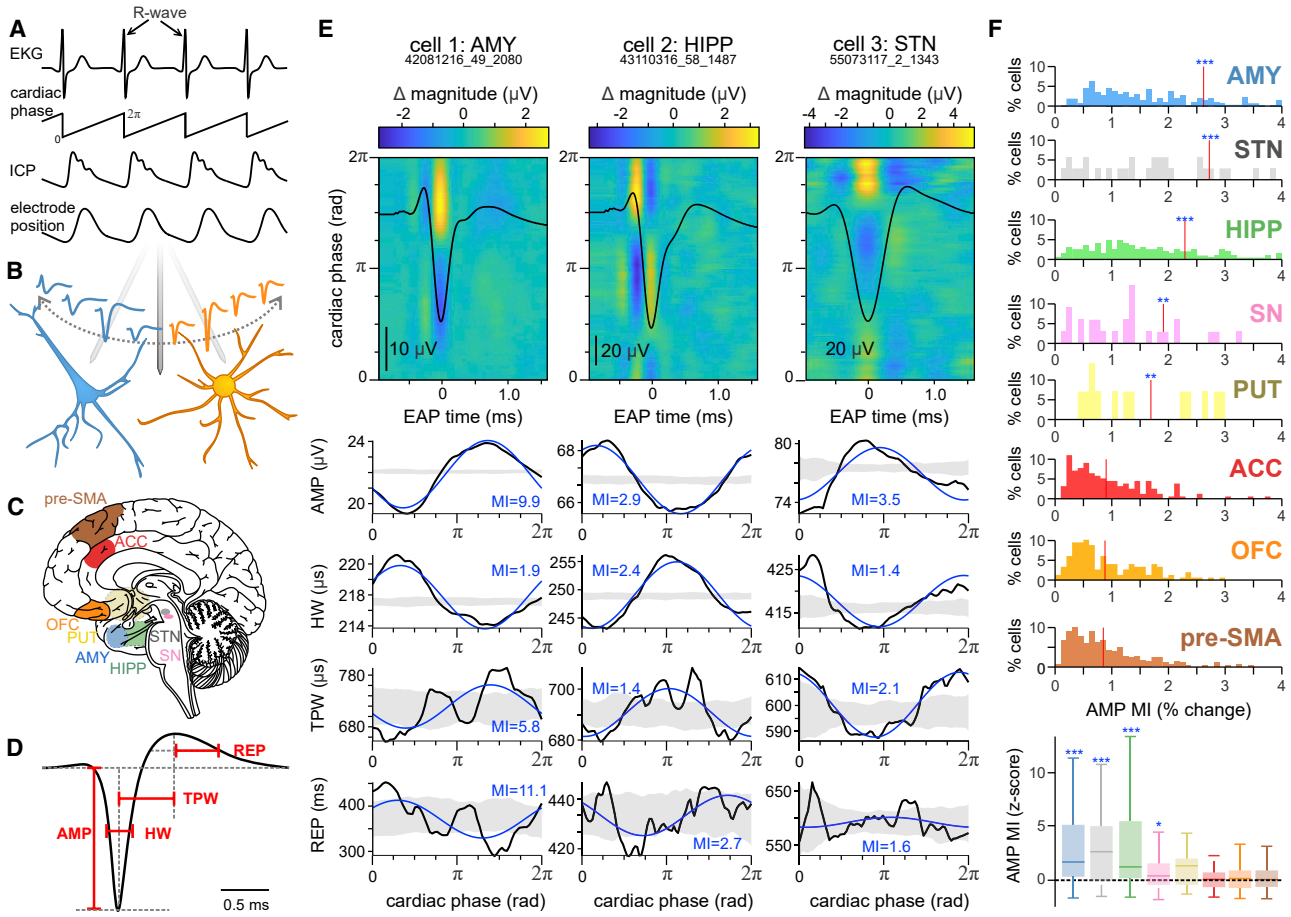

Figure 1. Extracellular Action Potential Waveforms in the Human Brain Are Modulated by the Cardiac Cycle

(A) Schematic showing the heartbeat monitored by electrocardiogram (EKG), the cardiac phase, the intracranial pressure (ICP), and the electrode position.

(B) The EAP at different locations for different cell types.

(C) Brain areas recorded *in vivo*.

(D) EAP waveform features.

(E) Three example units with cardiac-related EAP variability. Top: heatmaps show the change in EAP voltage relative to the mean EAP during the cardiac cycle (y axis). Mean EAP is overlaid in black (arbitrary position along the y axis). Bottom: black traces depict EAP features as a function of the cardiac cycle. Gray depicts the SD of 100 randomly shuffled bootstrapped samples (i.e., chance). Blue shows the fit of the circular linear regression used to derive the motion index (MI).

(F) Histograms show distributions of EAP AMP MI for all units in each recorded brain region (red lines: mean). Boxplots illustrate distribution (horizontal line = mean, box = first and third quartile, whisker = range) of AMP MI after Z scoring to shuffled waveforms. Brain areas with Z score >0 (t test) show significant AMP MI. *p < 0.05, **p < 0.01, ***p < 0.001

if AMP decreases by 10%, HW increases by 1.5%. Across the population, we found that HW negatively correlated with AMP (HW and AMP were linearly correlated for each neuron, and these correlation coefficients exceeded zero for the population; t test, t(1089) = −11.6, p = < 0.0001).

Variability in EAP Features during Cardiac Motion Reveals Three Cell Classes in the Human HIPP: NS, BS1, and BS2

Given that the motion-related effect on EAP waveforms is abundant in deep-brain structures, we next focused our analyses on the HIPP, a deep-brain region where, in rodents, numerous excitatory and inhibitory neural classes have been identified (Freund and Buzsáki, 1996; Graves et al., 2012; Hunt et al., 2018; Klausberger et al., 2003; Harris et al., 2018). We applied our analysis to the 69 units exhibiting the strongest cardiac-related AMP MI (the subset of cells with the strongest AMP modulation during the cardiac cycle, mean AMP MI = 4.1 ± 3.1; this subset was selected by comparing the EAP of an individual cell to the bootstrap shuffled waveforms at p < 0.05, STAR Methods). Although the remaining 114 hippocampal units had comparably weaker AMP MI (1.1 ± 0.7), these more weakly modulated units still exhibited statistically significant modulation as a group (t test, t(113) = 2.14, p = 0.03). In later parts of the paper (Figure 7), we apply the methods developed from the robust group of modulated neurons to the entire group of hippocampal units.

We clustered the EAP features of these 69 units in two ways: using standard features and with the inclusion of motion features. Standard features delineated units with narrow and

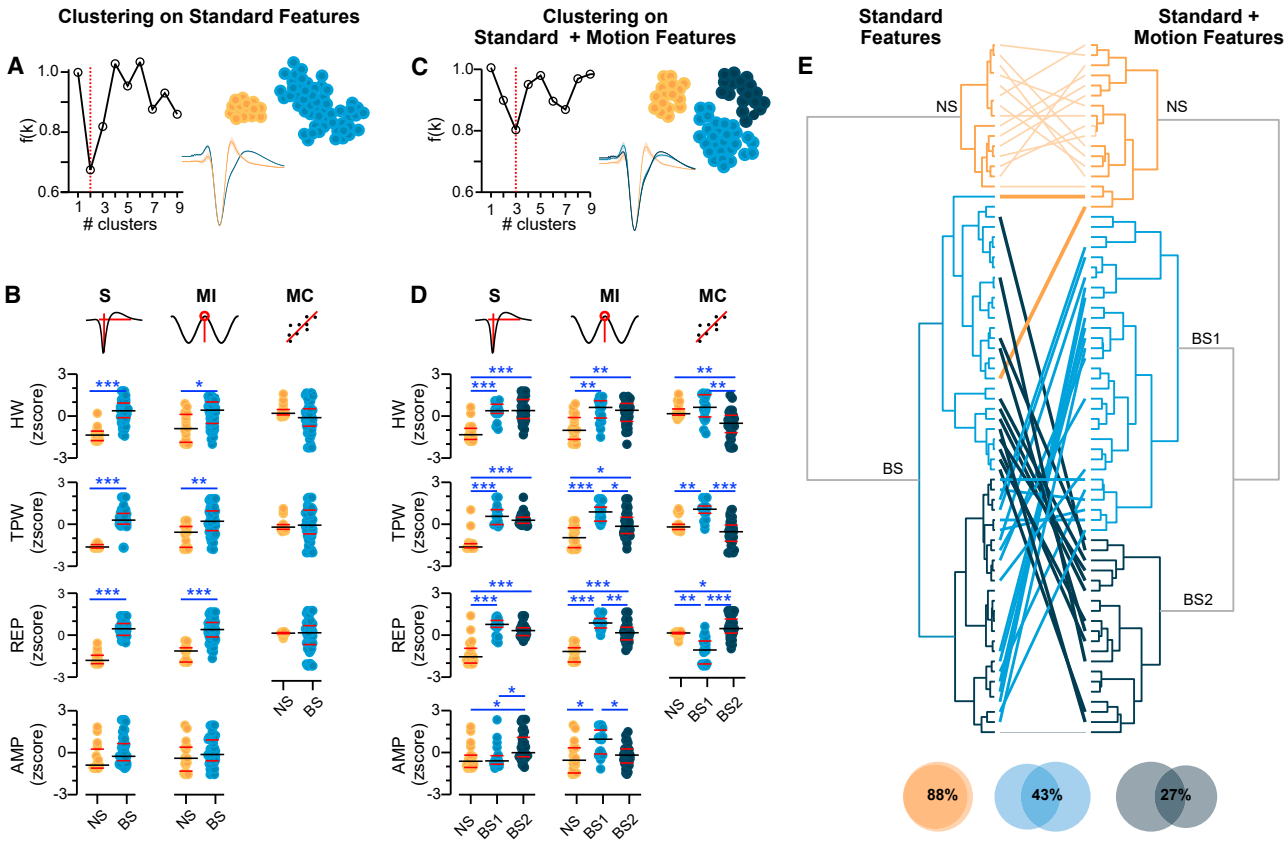

Figure 2. Motion Features Identify Three EAP Clusters in Human HIPP (NS, BS1, and BS2)

(A) K-means clustering of the standard features (HW, TPW, and REP of mean EAP). Left: density function f(k) identifies 2 clusters. Right: Features of NS (yellow) and BS cells (blue) plotted in t-distributed stochastic neighbor embedding (t-sne) feature space (van der Maaten and Hinton, 2008). Inset shows mean EAPs.

(B) EAP features for the clusters in A (each circle is a unit). Rows show the EAP features; columns show these features using standard methods (S), motion indices (MI), and motion correlations (MC). Only S features were used to cluster in (A) and (B), but we also plot MI and MC (black, mean; red, SEM; Wilcoxon rank sum tests).

(C) Including cardiac-related motion features (MI and MC) to the feature space reveals a third cluster, splitting the BS cells into BS1 (light blue) and BS2 (dark blue) sub-classes.

(D) Distribution of EAP features for the three clusters in (C).

(E) Dendrograms from hierarchical clustering on S features (left) and with the inclusion of MI and MC features (right). When the BS cells are forced into two groups in the S feature space (indicated by light versus dark blue color coding of the two BS branches on left side), these groups are not the same groups as those determined by the motion feature space (light and dark blue branches at right). Thick lines indicate relabeling of cells between the two feature-spaces. Venn Diagrams show percentage of cells that maintain labels in both feature sets. *$p < 0.05$, **$p < 0.01$, ***$p < 0.001$

broad EAP widths (Figures 2A and 2B; Figures S2A and S2B), henceforth, referred to as NS and BS units (comparison of width between NS and BS cells, respectively: HW = 0.225 ± 0.020 ms versus 0.272 ± 0.025 ms, rank sum $p = 1.02 \times 10^{-7}$; TPW = 0.348 ± 0.150 ms versus 0.740 ± 0.127 ms, $p = 1.8 \times 10^{-8}$; REP = 0.226 ± 0.140 ms versus 0.447 ± 0.070 ms, $p = 1.5 \times 10^{-7}$). Interestingly, a bimodal distribution of NS and BS cells was observed across different brain areas (see violin plots Figure S1B). The Hartigan's dip test of multimodality indicates that TPW (the most common metric used to distinguish NS and BS cells in humans and nonhuman primates) is significantly multimodal in ACC ($p = 0.048$), pre-SMA ($p = 0.0001$), and HIPP ($p < 0.0001$). Similarly, the distribution of TPW values is better explained by a mixture of two Gaussian distributions (bimodal) than a single Gaussian (unimodal) in ACC, AMY, HIPP, OFC, and pre-SMA.

While the standard EAP feature set identified two clusters of EAPs, the feature set including motion features (MI and MC) revealed three. Motion features split BS units into two groups: BS1 and BS2 (Figure 2C). While BS1 and BS2 units share standard features, their motion-related features differ (Figures 2C and 2D; e.g., TPW is more strongly negatively correlated with AMP for BS2 cells than BS1 cells). Even though BS1 and BS2 units originate from the same BS population, BS1 versus BS2 cannot be distinguished from standard EAP features alone. The optimal number of clusters in the standard space is 2, indicated by minimizing the f(k) density function (Figure 2A). However, forcing these units to cluster into three groups in the absence of motion features did not result in the same BS1 and

BS2 groups identified from the feature set accounting for motion (Figure S2C). Hierarchical clustering analysis illustrates that NS cells maintain their cluster labels in both the standard and motion feature sets, while BS units split into BS1 and BS2 only when utilizing motion features (Figure 2E). Of the 69 hippocampal units exhibiting the strongest EKG-related EAP variability, 18 were identified as NS (26%), 19 as BS1 (27%), and 32 as BS2 (46%).

It is possible that in some recording sessions the cardiac pulse is stronger, leading to greater electrode movement. We would expect this to be reflected in a greater EAP AMP MI. Among all three clusters, cardiac-related motion equally and significantly influenced the EAP AMP MI (t test of bootstrap *Z*-scored AMP MIs are different from zero, NS $t(17) = 4.53$, $p = 0.00029$; BS1 $t(18) = 5.77$, $p = 0.000018$; BS2 ($t(31) = 6.80$, $p = 1.28 \times 10^{-7}$; comparison of EAP AMP MI among cell types: ANOVA, $F(66,2) = 1.84$, $p = 0.168$). As a control, we assessed whether units belonging to different clusters were recorded simultaneously. Of 39 unique pairs of cells recorded on the same wire, 14 pairs (36%) were of different cell types (probability of recording each cell type simultaneously: p(NS and BS1) = 5%, p(NS and BS2) = 10%, p(BS1 and BS2) = 21%)). Of 269 unique pairs of cells recorded on the same bundle of wires on a hybrid electrode, 616 (55%), were pairs of different cell types (p(NS and BS1) = 9%, p(NS and BS2) = 9% p(BS1 and BS2) = 28%)). As BS1 and BS2 units can be recorded simultaneously on the same wires, it is unlikely that these reflect cell types from different regions of HIPP and, instead, are more likely to represent homogeneously dispersed cell types within a region (albeit, different regions of HIPP could have these cell types in different proportions).

While we largely focus on the HIPP we also tested our methodology in the AMY and STN, two brain areas with units exhibiting significant modulation in EAP AMP during the cardiac cycle (Figure 1F). Clustering with motion features revealed additional groupings in the AMY (Figure S3), a structure known for its plethora of distinct cell types (Millhouse and DeOlmos, 1983; Spampanato et al., 2011; Washburn and Moises, 1992). In contrast, we found no additional clusters in the STN (Figure S4), a structure that has a relatively homogeneous cytoarchitecture consisting largely of projection neurons (Yelnik and Percheron, 1979). Hence, large cardiac-related modulation in EAP features does not necessitate more unit clusters.

Biophysically Realistic Simulations Estimate the Cardiac-Related Motion at About 3 μm

We employed biophysically realistic single-neuron simulations of 10 spiny (SP) and 4 aspiny (AP) human neurons to understand how cardiac-related motion influences EAPs (Figure 3A). The three-stage optimization workflow to fit the biophysical models (Figure 3B) relies on two data modalities: the reconstructed morphology and the somatic electrophysiology responses from whole-cell patch-clamp experiments (Figure 3C; see STAR Methods). The multi-objective optimization procedure aims to minimize the sum of objectives (somatic electrophysiology features) resulting in the fit of a set of ionic conductances (free parameters; Figures 3D–3F). The outcome of this procedure are conductance-based single-neuron models reflecting *in vitro*, whole-cell patch-clamp recordings from cortical neurons obtained from tissue resected from the human temporal and frontal lobe of 11 patients (Table S3). The models capture the intracellular dynamics during spiking and offer the ability to simulate the EAP (Anastassiou et al., 2015; Gold et al., 2007, 2006; Jun et al., 2017; Schomburg et al., 2012; Taxidis et al., 2015).

We simulated cardiac-related motion in these models through "virtual" extracellular recordings. We selected a location ("recording electrode") within 100 μm from the soma of the model neuron and moved the location of this electrode to emulate the relative motion during the EKG period. Examples of simulations are shown for two models, one AP (Figure 4A) and one SP (Figure 4B). The modulation of EAP features during the simulated motion is qualitatively similar to *in vivo* recordings (e.g., compare Figures 4A and 4B to Figure 1E). We calculated the standard and motion-related EAP features for each model for 1–20 μm of simulated electrode motion. Figure 4C illustrates the feature space for 3 μm of relative motion (range selected for EAPs AMP-matched to those observed *in vivo*; 43.4 ± 24.8 μV). We compared the AMP and AMP MI modulation of our *in vivo* recordings to the model predictions and estimate that the microwires in our *in vivo* recordings are about 31.2 ± 15.6 μm away from the cell body (Figure 4D top) and transverse a relative distance of 3.45 ± 3.07 μm during the cardiac cycle (Figure 4D bottom).

Classifiers Indicate that NS Cells Are AP Neurons, while BS Cells Are SP

It remains unknown whether and how the recorded hippocampal units map onto cells of distinct types at the morphological or genetic level. We hypothesized that the properties of cells recorded *in vivo* could be predicted by mapping their EAP data into the model feature space, where we know both the morphological and electrophysiological cell type and can produce a simulated EAP signature. These models offer an ideal tool to test whether EAP features alone can differentiate between distinct (and known) cell types – if successful, these classifiers can be then applied on experimental EAP waveforms. To do so we implemented two approaches: (1) an experiment-based approach, and (2) a simulation-based approach.

In the experiment-based approach, we trained classifiers using the experimental EAP data and their associated EAP cluster labels, NS and BS (Figure 2). We then used these classifiers to predict the morphological type of the model neurons, AP and SP, solely based on EAP properties (see STAR Methods). We compared classifiers trained on different combinations of EAP features: (1) only standard EAP features, (2) standard + MI features, (3) standard + MI + MC features, and (4) only MI + MC features. Figure 5A shows the performance accuracy on experimental data left out in training. Confusion matrices indicate that standard features are required and sufficient to differentiate NS from BS units. Indeed, classifiers with standard features (S) perform as well as classifiers with motion features included (S + MI + MC) (cf. Figure 5A, S to S + MI + MC). Confirming this result, the beta coefficients of the dividing plane used by the classifier are high for standard EAP features, indicating their significant contribution to the separation between NS and BS units (i.e.,

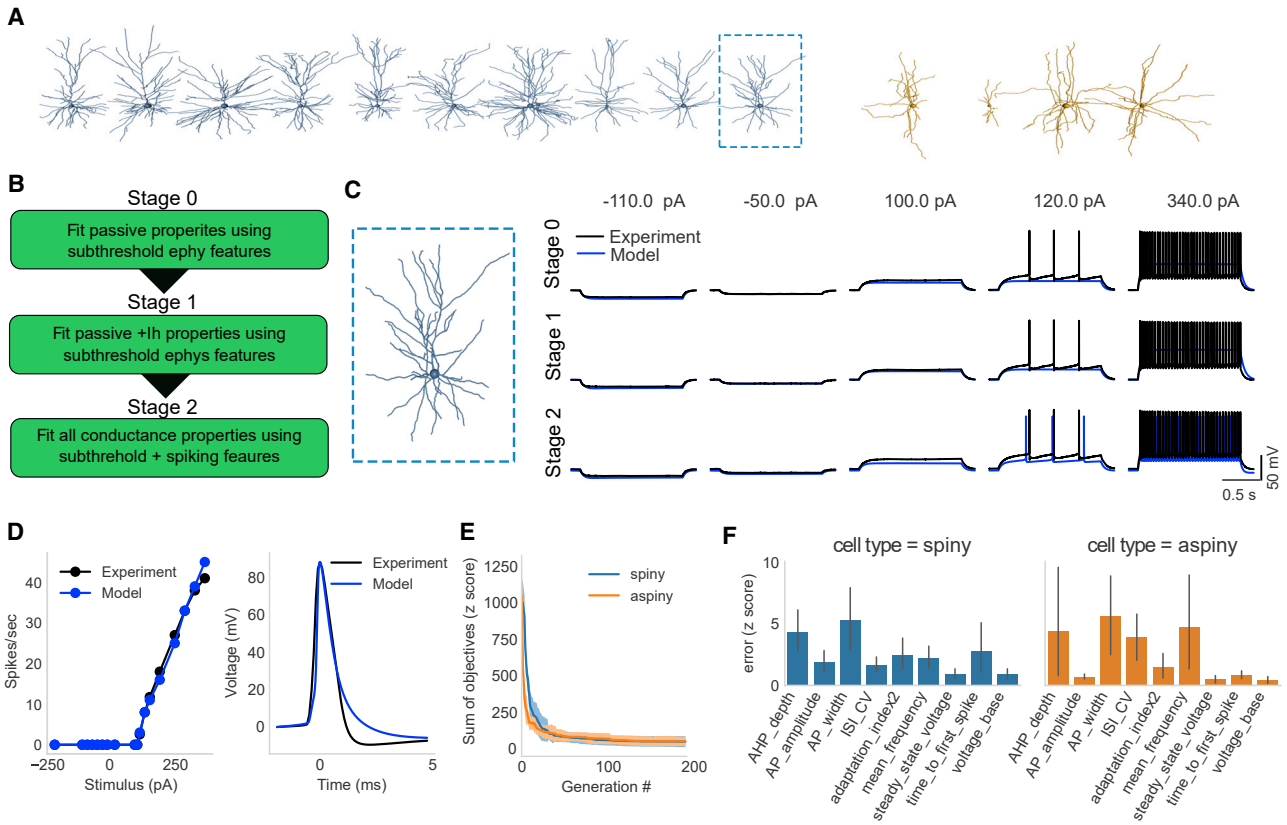

Figure 3. Optimization Workflow for Single-Cell All-Active Models of Human Cortical Neurons

(A) Reconstructed morphology of SP (blue) and AP (yellow) neurons.

(B) Three-stage optimization workflow.

(C) Optimization example (cell #571654895) extracted from human middle temporal gyrus. Left: neuron morphology (box indicates the cell in A). Right: results from each stage of optimization for different intracellular somatic stimulation (black, experiment trace; blue, model; left-to-right, increasing current amplitude).

(D) Comparison of current input versus spike rate (left) and somatic action potential waveform (right) between the experiment and model for the cell shown in C).

(E) Single-cell models become significantly better (i.e., capture the intracellular electrophysiology features of each experiment more faithfully) with increasing generation # following the genetic optimization used in stage 2 (mean ± SD across models).

(F) Training error (mean ± 95% confidence interval) for each electrophysiological feature (*Z*-scored difference between the average experimental and model electrophysiology features referenced to the experimental SD) for SP and AP models.

TPW, HW, REP; Figure 5B). When applying this classifier (trained on the standard experimental feature space) to the EAP feature space of the single-cell models, AP units were robustly classified as NS cells and SP units as BS cells, respectively (Figure 5C). This shows that a classifier trained on experimental data generalizes successfully to the model data.

In the simulation-based approach, we trained classifiers on the model EAP data using the ground truth label determined from the reconstructed morphologies of the human neurons (SP or AP; label based on morphological presence or absence of dendritic spines). The classifier that used standard features discriminated model AP and SP neurons with 84% accuracy (Figure 5D). We tested this simulation-based classifier on the experimentally recorded, hippocampal EAP waveforms. The majority (17/18, 94%) of neurons labeled experimentally as NS were classified as model AP neurons, while the majority (46/51, 90%) of neurons labeled BS were classified as SP. Thus, the simulation-based classifier, like the experiment-based classifier, robustly generalizes across feature spaces and attributes NS waveforms to AP neurons and BS waveforms to SP neurons.

Intrinsic Electrophysiological Properties of BS1 versus BS2 Neurons

Our analysis of motion-related EAP features indicates the presence of two BS classes, BS1 and BS2 (Figure 2C). What differentiates BS1 from BS2 units? To characterize the properties of BS1 versus BS2, we used simulation- and experiment-based approaches as above.

In the simulation-based approach, we "recorded" the EAP at 25 random locations around each human neuron model, simulating 3 μm of motion (i.e., the average motion estimated in Figure 4D; 10 model SP neurons were used from 8 patients). Cluster analysis on the EAP features of the SP models resulted in two groups: SP1 and SP2 (Figures 6A and 6B). The motion-related

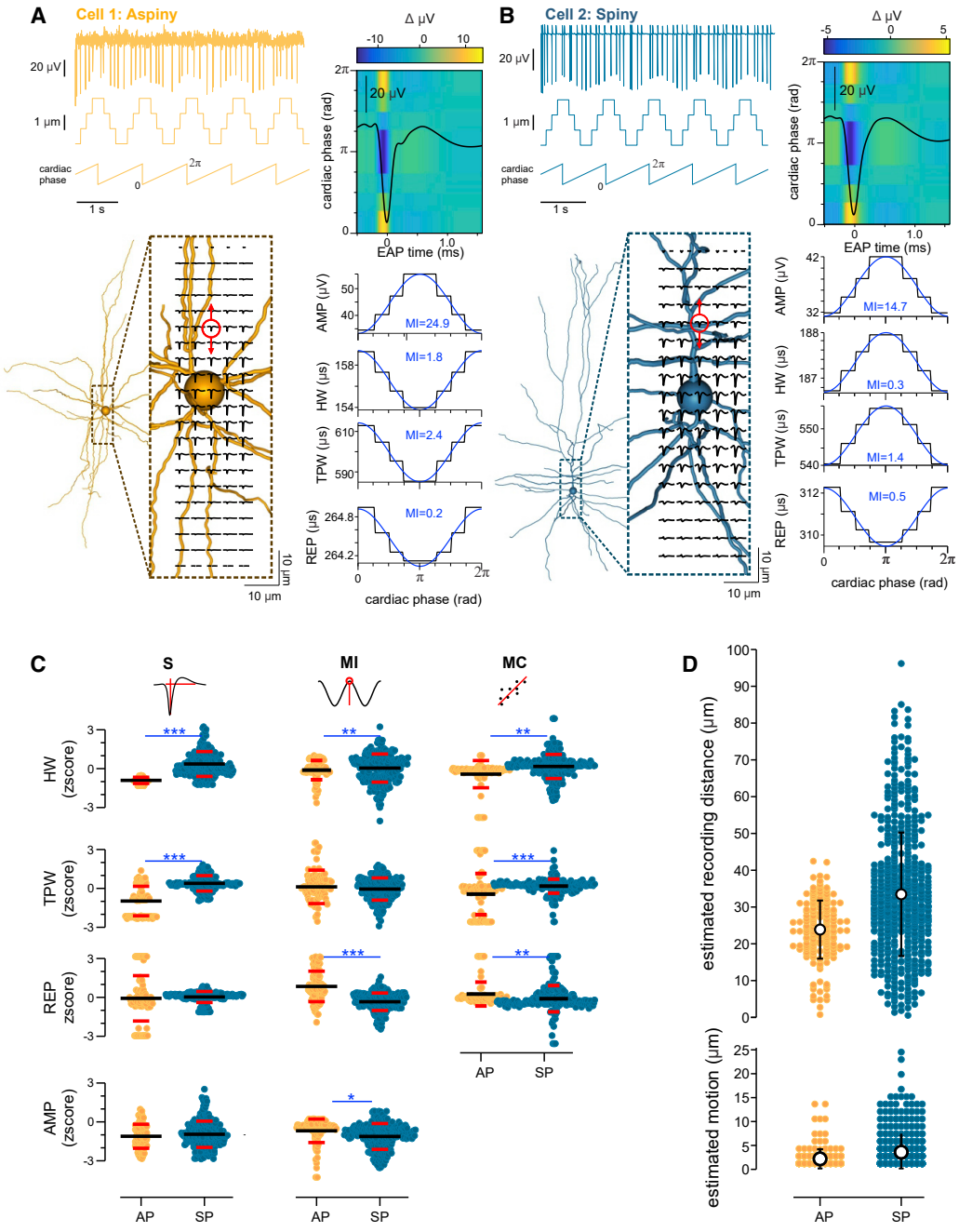

Figure 4. Simulated Electrode Motion in All-Active, Biophysically Realistic Models of Human Neurons

(A) Example model AP neuron. Cardiac-motion was simulated as a periodic change in the relative distance between soma and recording electrode. Left: simulated trace with 3 µm of cardiac-motion (red circle: recording location, arrows: direction of movement). Right: heatmap shows how the EAP varies as a function of the cardiac cycle (as in Figure 1E). Bottom: black traces show the variation in each feature during the simulated cardiac cycle; blue traces show the fit of a circular linear regression resulting in the modulation index (MI).

(B) Same as (A) for an example spiny neuron.

(C) Distribution of EAP features at 10 randomly selected locations around each AP (n = 4) and SP (n = 10) model neuron (black lines: mean, red lines: SEM; Wilcoxon rank sum tests). Each point indicates the EAP features at one spatial location.

(D) Estimated recording distance and motion of *in vivo* recordings. Mean distance and motion estimates do not significantly differ for AP or SP models (paired t test: distance p = 0.485, motion p = 0.346) (error bars = SD). *p < 0.05, **p < 0.01, ***p < 0.001

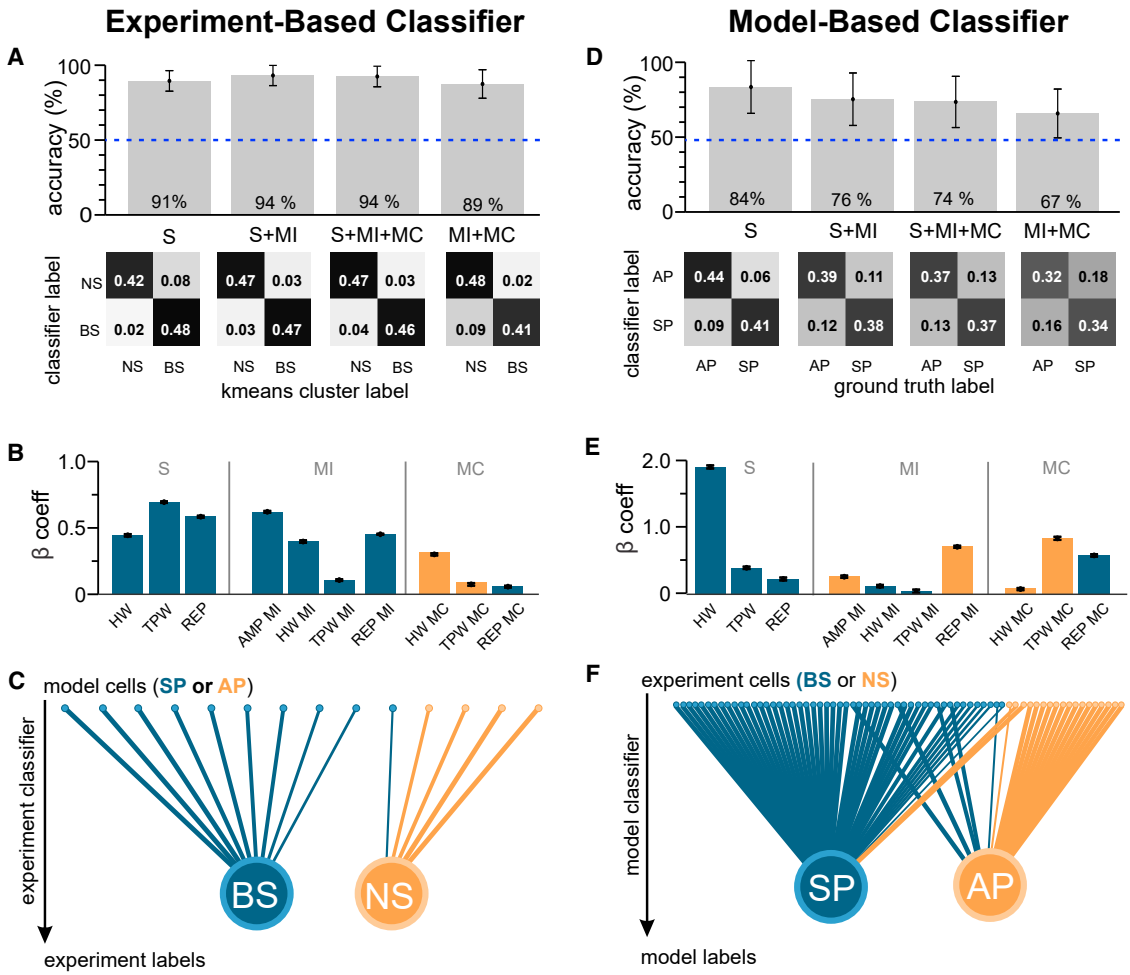

Figure 5. *In Vivo* NS and BS Units Map onto Single-Cell SP and AP Models

(A) Classifiers trained on *in vivo* data to discriminate between NS and BS units using combinations of S, MI, and MC features. Classifier performance was tested on a subset of left-out data and is depicted in confusion matrices and bar plots (box, mean; error: SD; blue line, chance).

(B) Beta coefficients of the S + MI + MC classifier (box, mean; error bar, SEM). Colors indicate whether the beta coefficient is larger for SP (blue) or AP (yellow) cells for a particular EAP feature.

(C) The classifier based on S features was applied to the simulated model-EAPs. Small circles (top) indicate model neurons (color-coded for SP, blue; or AP, yellow). Lines connect the circles to the labels given by the classifier. The width of the lines indicates the strength of the classification (i.e., how often the classifier converged on the same label for each EAP).

(D) Classifiers trained on EAP features to discriminate model AP and SP neurons.

(E) Beta coefficients of the model-based classifier.

(F) Same plotting conventions as in (C) but for applying the S-based model classifier to the *in vivo* experimental data.

features of the two clusters shared many similarities with those of BS1 and BS2 units recorded *in vivo*, e.g., B2 and SP2 exhibit strong negative correlations between HW/TPW and AMP (cf. Figures 2D and 6B, HW MC or TPW MC). While some model neurons (e.g., model #5, Figure 6C) exclusively gave rise to EAPs belonging to a single SP waveform cluster (in this case SP1), most models had EAPs in both clusters (e.g., 70% of the EAPs for model #1 belong to the SP1 cluster and 30% belong to the SP2 cluster). This lack of one-to-one mapping of EAP cluster-labels to each model occurs because the same neuron can elicit a spectrum of EAP waveforms, depending on the proximity of the recording electrode to the soma and dendrites (Gold et al., 2006). Mirroring the random location of extracellular recording locations in humans, we chose to label a model neuron as SP1 (or SP2) if the majority of its EAPs (>13/25 EAPs) belonged to the SP1 (or SP2) cluster. We identified 4 neurons as SP1 and the remaining 6 as SP2. We trained classifiers with these labels to identify model EAP waveforms as SP1 or SP2 (Figure S5). The classifier that utilized motion-based features performed with 20% higher accuracy on left-out test data than the classifier based on standard features alone (41% versus 62% respectively, Figure S5). These data illustrate that relative motion can uncover EAP features unique to individual classes and thereby facilitate classification of model cells.

In the experiment-based approach, we trained classifiers on the *in vivo* data using the BS1 versus BS2 cluster labels

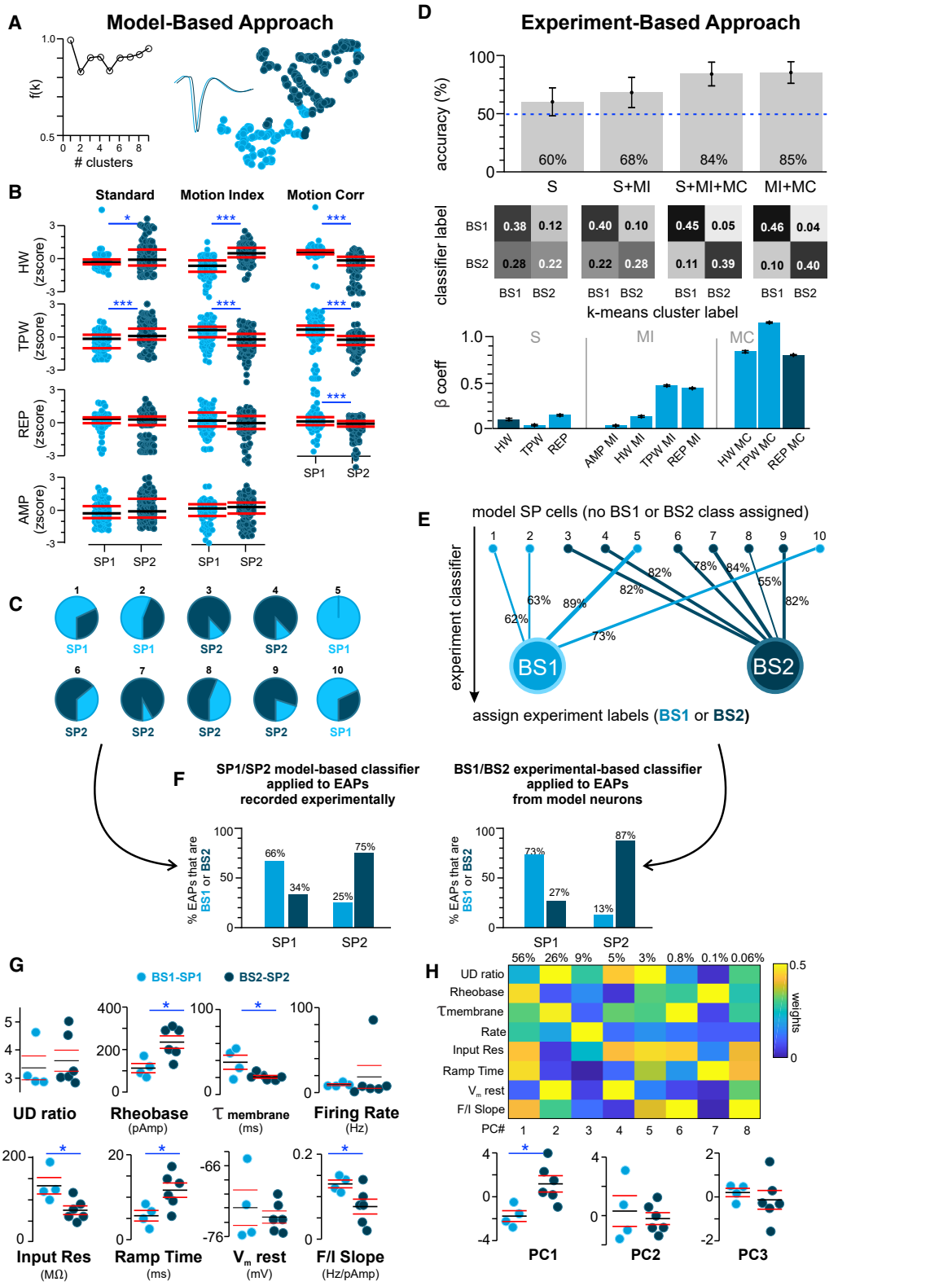

(legend on next page)

(Figure 2C) and a variety of EAP feature sets. Motion-related features supported the separation of BS1 and BS2 classes: classifiers using these features performed better (84% accuracy) compared to the classifier solely trained on standard features (60% accuracy; Figure 6D). Can classifiers trained exclusively on experimental EAP data predict the label of single-cell models? We applied the experimental-based BS1-BS2 classifier (including MC and MI features) to the SP-BS simulated EAP data and revealed that six model SP neurons are robustly identified as BS2, while the remaining four are classified as BS1 (Figure 6E).

Both the model- and experiment-based approach converge on the same result: BS1 and BS2 EAPs originate from two classes of neurons, namely, SP1 and SP2 (Figure 6F; the majority of BS1 and BS2 neurons are labeled as SP1 and SP2 both by the model- and experiment-based classifier). Yet, what is unique about the cellular properties of BS1-SP1 versus BS2-SP2 neurons that leads to such EAP feature- and motion-based separation? We analyzed multiple intracellular electrophysiological features (e.g., input resistance, firing rate) from the *in vitro* patch-clamp experiments each single-cell model was generated on. We found that SP2-BS2 cells exhibit a higher mean rheobase current, a lower input resistance, a longer spike ramp time, and lower membrane time constant compared to their SP1-BS1 counterparts (Figure 6G). Intriguingly, these 4 features account for the largest variance in the intrinsic feature space and together map onto the first component in PCA space (Figure 6H, scores of PC1 are significantly different for BS1-SP1 and BS2-SP2 cell types, t test, $p = 0.01$). This shows that the split of the BS class into BS1 and BS2 sub-classes is not arbitrary but maps onto neural classes with distinct intracellular features. Importantly, these intrinsic cellular properties cannot be measured directly *in vivo* in humans and are only accessible by bridging across data modalities, in our case via biophysically detailed modeling.

NS, BS1, and BS2 Cells Have Distinct *In Vivo* Properties during Endogenous Oscillations

Functionally distinct cell types uniquely coordinate their spikes to other classes and/or with respect to endogenous rhythms measured by the local field potential (LFP) (e.g., Klausberger et al., 2003; Klausberger and Somogyi, 2008). To pursue functional classification of human hippocampal NS, BS1, and BS2 neurons, we compared their *in vivo* spiking characteristics. We classified the entire population of 183 recorded hippocampal cells (i.e., this analysis is not restricted to only the strongly modulated cells) in a hierarchical fashion: by first applying the NS versus BS experiment-based classifier (Figure 5A) and then the BS1 versus BS2 model-based classifier (Figure 6D) to units identified as BS. Of the total population of 183 recorded hippocampal neurons, 49 were identified by the experimental classifier as NS (27%), 53 as BS1 (29%), and 81 as BS2 (44%). As with the original subset of 69 strongly modulated units, in this expanded set units of different cell classes were recorded by the same wire or wire bundle suggesting they are members of truly distinct cell types (72/145, 49%, unique pairs on same wire are of different cell types; 616/1,112, 55%, of pairs on same bundle are from different cell types; percentage of unique pairs that are BS1 and BS2 pairs, p(BS1 and BS2 same wire) = 27%, p(BS1 and BS2 same bundle) = 33%). NS, BS1, and BS2 units in the human HIPP exhibited similar low spike rates (NS: 1.6 ± 1.1 Hz, BS1: 1.2 ± 0.31 Hz, BS2: 1.4 ± 1.1 Hz, mean $\pm$ SD, ANOVA $F(2,176) = 0.47$, $p = 0.625$) with only 13/183 hippocampal cells (7%, 3 NS, 2 BS1, 8 BS2) having a mean rate that exceeded 10 Hz. Low spike rates are typical for human hippocampal (Rutishauser et al., 2008; Viskontas et al., 2007) and neocortical cells (Peyrache et al., 2012). BS1 and BS2 cells exhibit higher variability in their spike rates than NS cells (Figure 7A). Autocorrelograms indicate that this variability in spike rate is due in part to transient bursts of increased spiking activity of, on average, relatively quiescent cells (Figure 7A, burst index, Figure 7B). As a population, BS1 and BS2 cells are burstier than NS cells, which, in turn, exhibit uniform spike times (Figure 7B, bar plot; 57% of BS1 and BS2 cells are bursty compared to 35% of NS cells [bursty/not bursty × NS/BS, chi-square(1) = 6.56, $p = 0.0104$]; 22% of BS1 and BS2 cells fire with uniform rates compared to 51% of NS cells [uniform/not uniform × NS/BS, chi-square(1) = 12.66, $p = 0.0004$]).

We quantified spike-LFP synchrony with two measures: spike field coherence (SFC) and the Von Mises kappa value, an estimate of spike phase concentration. Human HIPP neurons exhibit

Figure 6. Two Types of Hippocampal Broad-Spike Waveform Cells (BS1 and BS2) Are Identified *In Vivo*

(A) K-means clustering on EAP features of model SP cells identifies two clusters: SP1 (light blue) and SP2 (dark blue). Density f(k) function, mean waveforms and t-sne plots of clusters as in Figure 2A.

(B) Distribution of EAP-features. (black line = mean, red line = SEM; Wilcoxon rank sum tests)

(C) Pie charts indicate the percentage of EAPs from each of the 10 SP models (25 EAPs sampled at different locations for each model) classified as SP1 (light blue) or SP2 (dark blue).

(D) S, MC, and MI features of *in vivo* EAPs were used to classify the experimental BS1 and BS2 clusters identified in Figure 2C. Same plotting conventions as Figure 5. Motion features (MI and MC) support classification of BS1 and BS2 experimental clusters; standard features alone (S) discriminate poorly between BS1 and BS2. (box: mean; error bar: SEM).

(E) The experiment-based classifier was applied to the EAPs from model SP neurons to provide BS1 and BS2 labels. Illustration conventions as in Figure 5C. 4 SP models are labeled BS1 and the remaining 6 are identified as BS2. The classifier was applied to the EAPs at 25 locations around each model (% of EAPs classified as BS1 or BS2 for each model is shown).

(F) Left: model-based classifier that identifies SP1 versus SP2 neurons classifies most experimental BS1 units as SP1 and most BS2 units as SP2. Right: the majority of EAPs originating from models identified as SP1 and SP2 in (A) are identified as BS1 and BS2 cells, respectively.

(G) Electrophysiological features of the model SP1-BS1 and SP2-BS2 neurons as determined from whole-cell patch-clamp experiments with human cortical neurons (black lines, mean; red lines, SEM; t tests).

(H) PCA applied to slice electrophysiological features depicted in (G). Colored matrix indicates feature weight for each component, and values at top show percentage of explained variance (t test, $p < 0.05$) (black lines = mean, red lines = SEM). *$p < 0.05$, **$p < 0.01$, ***$p < 0.001$

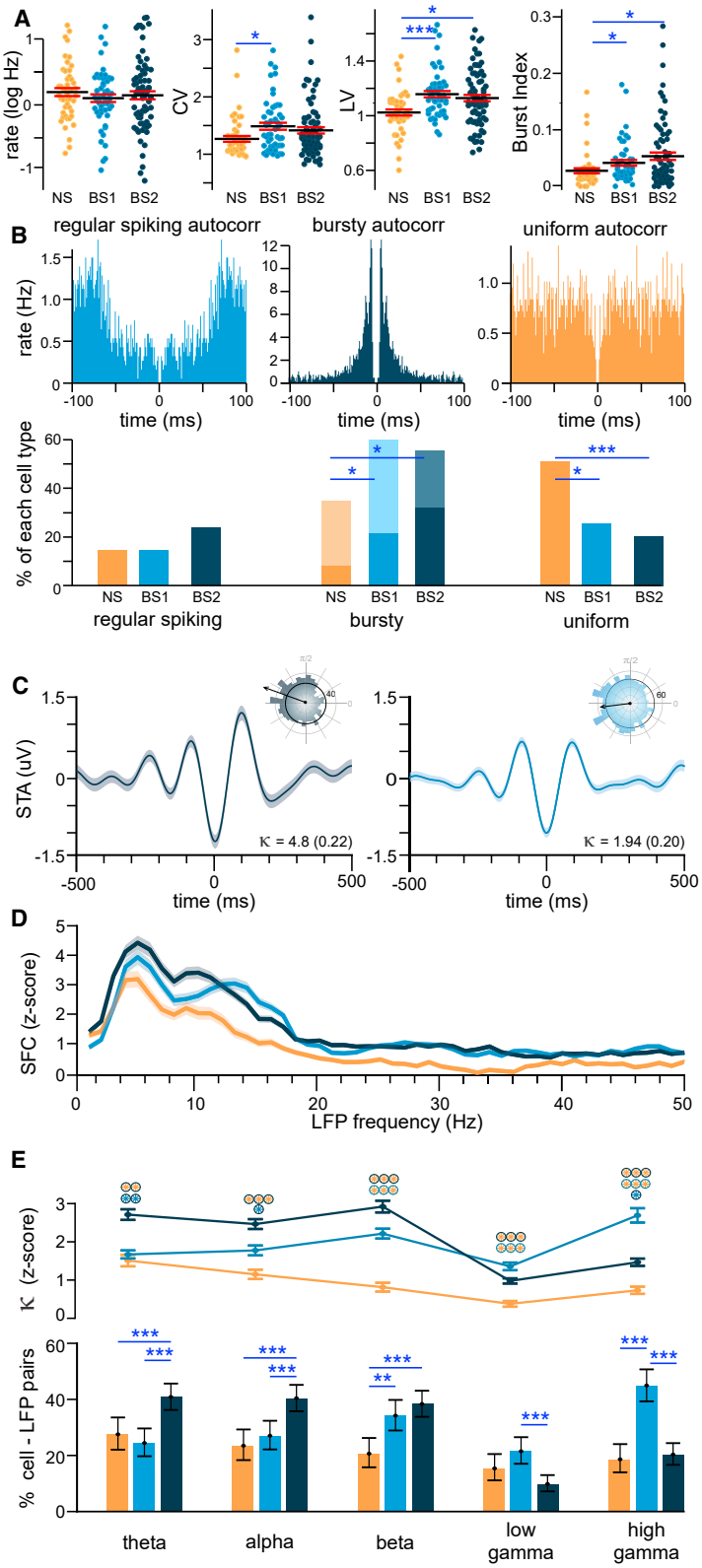

Figure 7. NS, BS1, and BS2 Cells in the Human HIPP Exhibit Distinct Spike Patterns and Phase Coupling Properties *In Vivo*

(A) Spike rate, coefficient of variation (CV), local variation (LV) (Shinomoto et al., 2003), and burst index of *in vivo* recorded NS (yellow), BS1 (light blue), and BS2 (dark blue) hippocampal neurons (black lines: mean; red lines: SEM, t tests).

(B) Example spike-train autocorrelograms of three units that represent three spiking profiles. Bar plots show percentage of NS, BS1, and BS2 cells identified as each type (scaled by total number of each cell type; bars of same color sum to 100%). The light and dark shading for bursty neurons indicates the percent of bursty cells using a lenient and strict burst criterion (STAR Methods) (chi-squared comparison of counts).

(C) Example spike triggered averages of theta-band filtered LFP signal for two simultaneously recorded cells: a BS2 cell (left) and a BS1 cell (right). Polar plots show the distribution of the LFP theta phase with arrow indicating the direction of phase concentration (lines, STA; shaded area, SEM) Kappa of phase concentration given as *Z*-scored values relative to shuffled data (raw values in parentheses).

(D) Population average spike-field coherence (SFC) and SEM across all neuron-LFP pairs. NS (yellow), BS1 (light blue), and BS2 cells (dark blue) (n = 41, 49, and 75 units, respectively).

(E) Line plot of mean ± SEM indicates the kappa value of the distribution of phases in each frequency band. Color of the center and encompassing circle indicates statistically significant comparison (t tests) between groups, e.g., a yellow center surrounded by a dark blue circle indicates that NS (yellow) and BS2 (dark blue) cells have different spike-LFP concentrations in an LFP frequency band. Bottom: percentage of single-unit LFP pairs for each cell class with significant spike-field phase concentrations in each frequency band (bar: percentage of significant pairs; error bar: 95% confidence interval for binomial random variable) (comparison of percent significant pairs between cell types, chi-squared). For example, the dark blue bar in theta indicates that 42% of BS2 unit-LFP pairs are synchronous in that band. *p < 0.05, **p < 0.01, ***p < 0.001

a high propensity to synchronize their spiking to local theta (Figures 7C–7E; 34% of the n = 992 unit-LFP pairs show significant phase concentrations as assessed by their kappa values; Figure 7E average of three bars with theta label). BS2 neurons are more likely to synchronize to local theta than BS1 or NS neurons (BS2 = 42%, NS = 28% and BS1 = 29%; Figure 7E), while BS1 cells exhibit enhanced coupling with low and high gamma oscillations (i.e., 43% BS1 cells fire at high gamma versus 19% BS2 and 18% NS). Furthermore, BS1 and BS2 are more likely to entrain to beta than NS (Figure 7E). Note that for the spike-field analysis we chose pairs of units and LFPs recorded on different neighboring electrodes; this ensures that the observed spike-field relationships remain unaffected by the EAP of a recorded unit contaminating low-frequency currents in the LFP (Anastassiou et al., 2015; Schomburg et al., 2012; Zanos et al., 2012). As an additional control, we repeated the analysis using only the subset of units from microwire bundles in which all three types were simultaneously recorded (n = 8 recording sessions, 115 cells) and observed similar effects (Figure S6). The differences in spike-field synchronization between cell types cannot be explained by differences in LFP. Indeed, across the population, the spike-triggered power is similar among different neuron types (Figure S6C).

We conclude that NS, BS1, and BS2 are distinct cell classes in the human HIPP that differ in their EAP waveform, their putative intrinsic properties, and their unique coupling characteristics to ongoing and functionally relevant hippocampal LFP oscillations. Importantly, the functional characteristics were not *a priori* included in the identification of these classes. Instead, they resulted as an unbiased prediction of the waveform-based classification that linked *in vivo* recordings to models with known intrinsic cellular properties.

DISCUSSION

We found that the EAP waveforms of neurons recorded with extracellular wires in the human brain *in vivo* exhibit small but robust and temporally periodic feature modulation during the cardiac cycle. This modulation occurs throughout the brain, with the strongest effects in deep-brain structures. These deep structures may be more susceptible to cardiac motion because of the dense bed of arteries at the base of the brain (Terem et al., 2018). While changes in EAP features due to cardiac-related motion have not been systematically documented in the human brain, cardioballistic motion effects are prominent in other electrophysiological and imaging techniques (e.g., EEG, [Srivastava et al., 2005], calcium imaging [Chen et al., 2012], functional imaging [Terem et al., 2018]). We show through biophysical simulations of human cortical neurons that a relative displacement of ~3 μm can account for the experimentally observed EAP waveform jitter. This estimate complements predictions of functional imaging in humans that estimate cardiac motion to be ~50 μm or less (Terem et al., 2018). The simulations also indicate that the distance between a neuron and a recording electrode is approximately 20–30 μm, an estimate in agreement with *in vitro* experiments (Anastassiou et al., 2015) and computational modeling (Gold et al., 2007, 2006; Taxidis et al., 2015). Although the estimated recording distance suggests a relatively narrow radius for isolating single units *in vivo* (~30 μm radius around the soma, scarcely twice the radius of most microwires), within this region the features of the EAP vary substantially. For example, within the 30 μm radius of a soma, the majority of EAPs exhibit an inverse relationship between EAP AMP and width features, an observation predicted by modeling data that can be explained by the active propagation of action potentials (Pettersen and Einevoll, 2008; Anastassiou et al., 2015; Gold et al., 2007, 2006).

We identified BS1 and BS2 cells by capitalizing on motion features caused by the heartbeat, but in principle the same classification could be achieved by intentionally introducing small amounts of motion in the brains of humans or other species (e.g., by micro-manipulating acute recording electrodes in cortex of rats or the archistriatum of zebra finches; Fee, 2000). We further predict that other bodily rhythms modulating intracranial pressure (e.g., the respiratory cycle) could be used to quantify motion-related changes in the EAP to identify novel cell classes. Given the recent interest in how rhythms of the body (respiratory, gastric, cardiac, circadian) modulate neural activity and cognition (e.g., Heck et al., 2017; Tort et al., 2018; Zelano et al., 2016; Kern et al., 2013; Kim et al., 2019; Pedemonte et al., 2003), a future set of experiments will need to carefully characterize how bodily rhythms influence EAP waveforms, spike detection, spike sorting, and the resulting cell classification.

We defined three classes based on EAP features, NS, BS1, and BS2, that also differ in their *in vivo* spike characteristics as well as their predicted intrinsic cellular properties. The narrow-width EAP waveform and decreased spike rate variability of NS units (robustly classified in our analysis as AP neurons) is strongly reminiscent of inhibitory interneurons and basket cells (e.g., Barthó et al., 2004, Joshi and Hawken, 2006; Krimer et al., 2005; McCormick et al., 1985; Gouwens et al., 2019; Anastassiou et al., 2015). But what about the differences between BS classes, BS1 versus BS2? The inverse relationship between rheobase versus input resistance and ramp time points to BS1 neurons being electrotonically more compact than BS2. BS1 neurons also possess a considerably increased (i.e., roughly double) membrane time constant over their BS2 counterparts, suggesting they are more responsive to fast oscillatory input (Eyal et al., 2016; Koch, 2004), an observation also supported by the spike-field analysis (see below). The lower membrane time constant of BS2 neurons allows their membrane potential to be more easily entrained by slower synaptic input. BS1 versus BS2 EAP waveforms are indistinguishable when considering standard EAP features (but, crucially, are separable by their motion-related EAP features) suggesting that their short-term spike dynamics are supported by similar mechanisms (i.e., transient Na^+ and K^+ currents that shape the AP waveform in the ~2 ms window discernable by extracellular recordings are indistinguishable in the two BS classes). Slower K^+ and Ca^{2+}-dependent conductances affect slower components of the EAP waveform and contribute to slower spike-related mechanisms such as adaptation (Anastassiou et al., 2015).

We find that AP NS units are entrained to a broad range of frequencies (from theta to high gamma), indicative of general inhibition (Fellous et al., 2001; Hasenstaub et al., 2005), whereas BS2 cells phase lock preferably to slower theta and alpha

rhythms and BS1 cells preferably entrain to faster gamma oscillations. Such cell-class-specific entrainment is consistent with the intrinsic properties of the two classes. While the electrotonic compactness of BS1 cells renders them ideal for integrating faster synaptic drive, the increased membrane time constant of BS2 cells makes them more susceptible to slower synaptic drive (notably, in our work the intrinsic properties of BS classes are determined independently from phase-locking characteristics). Continuous rhythmic firing units versus clustered rhythmically firing units covering the theta band have been reported in human HIPP and are reminiscent of BS1- versus BS2-type activity (Isokawa-Akesson et al., 1987).

A possible limitation in ascribing specific intrinsic properties to BS1 versus BS2 neurons such as input resistance and rheobase is the use of neuron models derived from human neocortex rather than HIPP. The main challenge is the lack of morphological and electrophysiological single-neuron data from human single neurons from identified brain regions beyond human neocortex to allow the development of biophysically faithful and region-specific single-neuron models. Even so, we assess this limitation as relatively inconsequential toward our conclusions. Specifically, separation of BS *in vivo* units into BS1 versus BS2 in our work can be solely achieved based on feature modulation and does not depend on identifying intrinsic properties of each cell type. Yet, the fact that conclusions derived separately from the experimental- and simulation-based approach such as BS1 versus BS2 and SP1 versus SP2 cluster compositions are in such close agreement offers confidence in the model-based predictions. Regarding the estimation of intrinsic properties, while in rodents pyramidal neurons can exhibit differences, they also share many properties like an extended dendritic morphology, spike generation, and support mechanisms along their cables (Spruston, 2008), and distinct molecular markers (e.g., calcium/calmodulin-dependent protein kinase, which is present in both hippocampal and neocortical pyramidal cells ([Erondu and Kennedy, 1985]). We expect EAP features captured by the human neocortical models to be a reflection of these shared commonalities, while dissection of even finer, region-specific cell-type-differences requires a dedicated set of *in vitro* experiments and effort toward specific model development.

Our analysis focuses on four EAP waveform metrics (AMP, HW, TPW, and REP), because (1) they are general standards for cell classification in the *in vivo* literature, and (2) the use of these features allows for a common feature space between the model and *in vivo* data. We encountered several challenges in relating the model and experimental-feature spaces, e.g., matching the recording filters in the model with those of the *in vivo* hardware and software, applying the same feature detection methods to both model and *in vivo* data, accounting for the impact of inherent background noise in the *in vivo* data that is absent in the modeling data. Because our models are based on reconstructions of *in vitro* recordings, we optimized not only the spiking properties of the cell model (spike timing, spike rate) given a particular morphology but also the intracellular action potential waveform, especially the EAP AMP and HW. Indeed, because HW is included in the optimization workflow and strongly matches the *in vitro* recordings, it is a major feature in discriminating cell classes in both the model and experimental space (Figure 5E).

While here we focus on the human HIPP, our overall approach is applicable to other brain areas and other species where EAPs are jittered by relative motion; in the case of cardiac motion we showed evidence in other deep structures like the AMY and STN. Furthermore, we showed how biophysical models can be used to link to seemingly dissociated datasets (*in vitro* physiology and morphology reconstructions with *in vivo* recordings of unit activity and LFPs) to offer insights into the identity and unique properties of recorded neurons. We view this approach as a promising means toward data reconciliation, cell classification, and functional interpretation particularly in human brain circuits where most of the multi-modal experimentation attainable in animal models remains unfeasible.

STAR★METHODS

Detailed methods are provided in the online version of this paper and include the following:

- KEY RESOURCES TABLE
- LEAD CONTACT AND MATERIALS AVAILABILITY
- EXPERIMENTAL MODEL AND SUBJECT DETAILS
- METHOD DETAILS
  - *In vivo* neural recordings with cardiac monitoring
  - All-active single-neuron models with motion simulation
- QUANTIFICATION AND STATISTICAL ANALYSIS
  - Spike detection and sorting of single units
  - Single unit firing properties and coherence with LFPs
  - Quantification of EAP waveform features
  - Identification of EAP waveform clusters using PCA and k-means clustering
  - SVM Classification of EAPS
- DATA CODE AND AVAILABILITY

SUPPLEMENTAL INFORMATION

Supplemental Information can be found online at https://doi.org/10.1016/j.celrep.2020.02.027.

ACKNOWLEDGMENTS

We wish to thank the Allen Institute founder, Paul G. Allen, for his vision, encouragement, and support. We thank all members of the Anastassiou and Rutishauser labs for discussions, Shannon Sullivan, April Carlson, and Nand Chandravadia for their assistance in spike sorting, Anatoly Buchin and Tom Chartrand for their contributions to the optimization and simulation workflow, and Uygar Sümbül for critical comments and discussions. We gratefully acknowledge the willingness of our patients to participate in this study and the staff and physicians of the Epilepsy Monitoring Unit and the Movement Disorders Program at Cedars-Sinai Medical Center for their invaluable assistance. Research reported in this publication was supported by the National Institute of Mental Health, United States (R01MH110831 to U.R.) and the National Institute of Neurological Disorders and Stroke, United States (U01NS103792, U01NS098961 to U.R.).

AUTHOR CONTRIBUTIONS

C.P.M., J.K., A.N.M., and U.R. designed *in vivo* experiments and collected *in vivo* extracellular data. A.N., Y.W., and C.A.A. constructed the all-active

human single-neuron models and simulated data. A.N.M. performed surgery and provided patient care. C.P.M. and Y.W. performed data analysis with guidance from C.A.A. and U.R. J.K. first noticed the cardiac-related changes in the electrophysiology. C.P.M. wrote the initial draft of the manuscript. All authors discussed the results at all stages of the project and contributed to the final manuscript.

DECLARATION OF INTERESTS

The authors declare no competing interests.

Received: September 9, 2019
Revised: December 23, 2019
Accepted: February 5, 2020
Published: March 10, 2020

REFERENCES

Aevermann, B.D., Novotny, M., Bakken, T., Miller, J.A., Diehl, A.D., Osumi-Sutherland, D., Lasken, R.S., Lein, E.S., and Scheuermann, R.H. (2018). Cell type discovery using single-cell transcriptomics: implications for ontological representation. Hum. Mol. Genet. *27* (*R1*), R40–R47.

Allen, J.J.B., Chambers, A.S., and Towers, D.N. (2007). The many metrics of cardiac chronotropy: a pragmatic primer and a brief comparison of metrics. Biol. Psychol. *74*, 243–262.

Anastassiou, C.A., and Shai, A.S. (2016). Psyche, signals and systems. In Micro-, Meso- and Macro-Dynamics of the Brain, G. Buzsáki and Y. Christen, eds. (Springer).

Anastassiou, C.A., Perin, R., Buzsáki, G., Markram, H., and Koch, C. (2015). Cell type- and activity-dependent extracellular correlates of intracellular spiking. J. Neurophysiol. *114*, 608–623.

Ardid, S., Vinck, M., Kaping, D., Marquez, S., Everling, S., and Womelsdorf, T. (2015). Mapping of functionally characterized cell classes onto canonical circuit operations in primate prefrontal cortex. J. Neurosci. *35*, 2975–2991.

Barthó, P., Hirase, H., Monconduit, L., Zugaro, M., Harris, K.D., and Buzsáki, G. (2004). Characterization of neocortical principal cells and interneurons by network interactions and extracellular features. J. Neurophysiol. *92*, 600–608.

Berens, P. (2009). CircStat: A MATLAB Toolbox for Circular Statistics. J. Stat. Softw. *31*, 1–21.

Buzsáki, G. (2004). Large-scale recording of neuronal ensembles. Nat. Neurosci. *7*, 446–451.

Buzsáki, G. (2006). Rhythms of the Brain (Oxford University Press).

Buzsáki, G., and Draguhn, A. (2004). Neuronal oscillations in cortical networks. Science *304*, 1926–1929.

Buzsáki, G., Penttonen, M., Nádasdy, Z., and Bragin, A. (1996). Pattern and inhibition-dependent invasion of pyramidal cell dendrites by fast spikes in the hippocampus in vivo. Proc. Natl. Acad. Sci. USA *93*, 9921–9925.

Buzsáki, G., Anastassiou, C.A., and Koch, C. (2012). The origin of extracellular fields and currents–EEG, ECoG, LFP and spikes. Nat. Rev. Neurosci. *13*, 407–420.

Carlson, A.A., Rutishauser, U., and Mamelak, A.N. (2018). Safety and Utility of Hybrid Depth Electrodes for Seizure Localization and Single-Unit Neuronal Recording. Stereotact. Funct. Neurosurg. *96*, 311–319.

Chen, X., Leischner, U., Varga, Z., Jia, H., Deca, D., Rochefort, N.L., and Konnerth, A. (2012). LOTOS-based two-photon calcium imaging of dendritic spines *in vivo*. Nat. Protoc. *7*, 1818–1829.

Connors, B.W., and Gutnick, M.J. (1990). Intrinsic firing patterns of diverse neocortical neurons. Trends Neurosci. *13*, 99–104.

DeFelipe, J., López-Cruz, P.L., Benavides-Piccione, R., Bielza, C., Larrañaga, P., Anderson, S., Burkhalter, A., Cauli, B., Fairén, A., Feldmeyer, D., et al. (2013). New insights into the classification and nomenclature of cortical GABAergic interneurons. Nat. Rev. Neurosci. *14*, 202–216.

Erondu, N.E., and Kennedy, M.B. (1985). Regional distribution of type II Ca2+/calmodulin-dependent protein kinase in rat brain. J. Neurosci. *5*, 3270–3277.

Eyal, G., Verhoog, M.B., Testa-Silva, G., Deitcher, Y., Lodder, J.C., Benavides-Piccione, R., Morales, J., DeFelipe, J., de Kock, C.P., Mansvelder, H.D., and Segev, I. (2016). Unique membrane properties and enhanced signal processing in human neocortical neurons. eLife *5*, Published online October 6, 2016. https://doi.org/10.7554/eLife.16553.

Faraut, M.C.M., Carlson, A.A., Sullivan, S., Tudusciuc, O., Ross, I., Reed, C.M., Chung, J.M., Mamelak, A.M., and Rutishauser, U. (2018). Dataset of human medial temporal lobe single neuron activity during declarative memory encoding and recognition. Sci. Data *5*, 180010. https://doi.org/10.1038/sdata.2018.10.

Fee, M.S. (2000). Active stabilization of electrodes for intracellular recording in awake behaving animals. Neuron *27*, 461–468.

Fellous, J.-M., Houweling, A.R., Modi, R.H., Rao, R.P., Tiesinga, P.H., and Sejnowski, T.J. (2001). Frequency dependence of spike timing reliability in cortical pyramidal cells and interneurons. J. Neurophysiol. *85*, 1782–1787.

Freund, T.F., and Buzsáki, G. (1996). Interneurons of the hippocampus. Hippocampus *6*, 347–470.

Fries, P., Reynolds, J.H., Rorie, A.E., and Desimone, R. (2001). Modulation of oscillatory neuronal synchronization by selective visual attention. Science *291*, 1560–1563.

Gold, C., Henze, D.A., Koch, C., and Buzsáki, G. (2006). On the origin of the extracellular action potential waveform: A modeling study. J. Neurophysiol. *95*, 3113–3128.

Gold, C., Henze, D.A., and Koch, C. (2007). Using extracellular action potential recordings to constrain compartmental models. J. Comput. Neurosci. *23*, 39–58.

González-Burgos, G., Miyamae, T., Krimer, Y., Gulchina, Y., Pafundo, D.E., Krimer, O., Bazmi, H., Arion, D., Enwright, J.F., Fish, K.N., and Lewis, D.A. (2019). Distinct Properties of Layer 3 Pyramidal Neurons from Prefrontal and Parietal Areas of the Monkey Neocortex. J. Neurosci. *39*, 7277–7290.

Gouwens, N.W., Sorensen, S.A., Berg, J., Lee, C., Jarsky, T., Ting, J., Sunkin, S.M., Feng, D., Anastassiou, C.A., Barkan, E., et al. (2019). Classification of electrophysiological and morphological neuron types in the mouse visual cortex. Nat. Neurosci. *22*, 1182–1195.

Gratiy, S.L., Billeh, Y.N., Dai, K., Mitelut, C., Feng, D., Gouwens, N.W., Cain, N., Koch, C., Anastassiou, C.A., and Arkhipov, A. (2018). BioNet: A Python interface to NEURON for modeling large-scale networks. PLoS ONE *13*, e0201630.

Graves, A.R., Moore, S.J., Bloss, E.B., Mensh, B.D., Kath, W.L., and Spruston, N. (2012). Hippocampal pyramidal neurons comprise two distinct cell types that are countermodulated by metabotropic receptors. Neuron *76*, 776–789.

Gray, C.M., and McCormick, D.A. (1996). Chattering cells: superficial pyramidal neurons contributing to the generation of synchronous oscillations in the visual cortex. Science *274*, 109–113.

Harris, K.D., Hochgerner, H., Skene, N.G., Magno, L., Katona, L., Bengtsson Gonzales, C., Somogyi, P., Kessaris, N., Linnarsson, S., and Hjerling-Leffler, J. (2018). Classes and continua of hippocampal CA1 inhibitory neurons revealed by single-cell transcriptomics. PLoS Biol. *16*, e2006387.

Hasenstaub, A., Shu, Y., Haider, B., Kraushaar, U., Duque, A., and McCormick, D.A. (2005). Inhibitory postsynaptic potentials carry synchronized frequency information in active cortical networks. Neuron *47*, 423–435.

Heck, D.H., McAfee, S.S., Liu, Y., Babajani-Feremi, A., Rezaie, R., Freeman, W.J., Wheless, J.W., Papanicolaou, A.C., Ruszinkó, M., Sokolov, Y., and Kozma, R. (2017). Breathing as a Fundamental Rhythm of Brain Function. Front. Neural Circuits *10*, 115.

Hodge, R.D., Bakken, T.E., Miller, J.A., Smith, K.A., Barkan, E.R., Graybuck, L.T., Close, J.L., Long, B., Penn, O., Yao, Z., et al. (2018). Conserved cell types with divergent features between human and mouse cortex (preprint). Neuroscience *573*, 61–68.

Holt, G.R., and Koch, C. (1999). Electrical interactions via the extracellular potential near cell bodies. J. Comput. Neurosci. *6*, 169–184.

Hunt, D.L., Linaro, D., Si, B., Romani, S., and Spruston, N. (2018). A novel pyramidal cell type promotes sharp-wave synchronization in the hippocampus. Nat. Neurosci. *21*, 985–995.

Hunt, D.L., Lai, C., Smith, R.D., Lee, A.K., Harris, T.D., and Barbic, M. (2019). Multimodal *in vivo* brain electrophysiology with integrated glass microelectrodes. Nat. Biomed. Eng. *3*, 741–753.

Isokawa-Akesson, M., Wilson, C.L., and Babb, T.L. (1987). Diversity in periodic pattern of firing in human hippocampal neurons. Exp. Neurol. *98*, 137–151.

Ison, M.J., Mormann, F., Cerf, M., Koch, C., Fried, I., and Quiroga, R.Q. (2011). Selectivity of pyramidal cells and interneurons in the human medial temporal lobe. J. Neurophysiol. *106*, 1713–1721.

Jia, X., Siegle, J.H., Bennett, C., Gale, S.D., Denman, D.J., Koch, C., and Olsen, S.R. (2019). High-density extracellular probes reveal dendritic backpropagation and facilitate neuron classification. J. Neurophysiol. *121*, 1831–1847.

Johnston, K., DeSouza, J.F.X., and Everling, S. (2009). Monkey prefrontal cortical pyramidal and putative interneurons exhibit differential patterns of activity between prosaccade and antisaccade tasks. J. Neurosci. *29*, 5516–5524.

Joshi, S., and Hawken, M.J. (2006). Loose-patch-juxtacellular recording *in vivo*–a method for functional characterization and labeling of neurons in macaque V1. J. Neurosci. Methods *156*, 37–49.

Jun, J.J., Mitelut, C., Lai, C., Gratiy, S.L., Anastassiou, C.A., and Harris, T.D. (2017). Real-time spike sorting platform for high-density extracellular probes with ground-truth validation and drift correction. bioRxiv. https://doi.org/10.1101/101030.

Kamiński, J., Sullivan, S., Chung, J.M., Ross, I.B., Mamelak, A.N., and Rutishauser, U. (2017). Persistently active neurons in human medial frontal and medial temporal lobe support working memory. Nat. Neurosci. *20*, 590–601.

Kamiński, J., Mamelak, A.N., Birch, K., Mosher, C.P., Tagliati, M., and Rutishauser, U. (2018). Novelty-Sensitive Dopaminergic Neurons in the Human Substantia Nigra Predict Success of Declarative Memory Formation. Curr. Biol. *28*, 1333–1343.

Kern, M., Aertsen, A., Schulze-Bonhage, A., and Ball, T. (2013). Heart cycle-related effects on event-related potentials, spectral power changes, and connectivity patterns in the human ECoG. Neuroimage *81*, 178–190.

Kim, K., Ladenbauer, J., Babo-Rebelo, M., Buot, A., Lehongre, K., Adam, C., Hasboun, D., Lambrecq, V., Navarro, V., Ostojic, S., and Tallon-Baudry, C. (2019). Resting-State Neural Firing Rate Is Linked to Cardiac-Cycle Duration in the Human Cingulate and Parahippocampal Cortices. J. Neurosci. *39*, 3676–3686.

Klausberger, T., and Somogyi, P. (2008). Neuronal diversity and temporal dynamics: the unity of hippocampal circuit operations. Science *321*, 53–57.

Klausberger, T., Magill, P.J., Márton, L.F., Roberts, J.D.B., Cobden, P.M., Buzsáki, G., and Somogyi, P. (2003). Brain-state- and cell-type-specific firing of hippocampal interneurons *in vivo*. Nature *421*, 844–848. https://doi.org/10.1038/nature01374.

Koch, C. (2004). Biophysics of Computation: Information Processing in Single Neurons (Oxford University Press).

Kohara, K., Pignatelli, M., Rivest, A.J., Jung, H.-Y., Kitamura, T., Suh, J., Frank, D., Kajikawa, K., Mise, N., Obata, Y., et al. (2014). Cell type-specific genetic and optogenetic tools reveal hippocampal CA2 circuits. Nat. Neurosci. *17*, 269–279.

Krimer, L.S., Zaitsev, A.V., Czanner, G., Kröner, S., González-Burgos, G., Povysheva, N.V., Iyengar, S., Barrionuevo, G., and Lewis, D.A. (2005). Cluster analysis-based physiological classification and morphological properties of inhibitory neurons in layers 2-3 of monkey dorsolateral prefrontal cortex. J. Neurophysiol. *94*, 3009–3022.

Logothetis, N.K., Kayser, C., and Oeltermann, A. (2007). In vivo measurement of cortical impedance spectrum in monkeys: implications for signal propagation. Neuron *55*, 809–823.

Markram, H., Toledo-Rodriguez, M., Wang, Y., Gupta, A., Silberberg, G., and Wu, C. (2004). Interneurons of the neocortical inhibitory system. Nat. Rev. Neurosci. *5*, 793–807.

McCormick, D.A., Connors, B.W., Lighthall, J.W., and Prince, D.A. (1985). Comparative electrophysiology of pyramidal and sparsely spiny stellate neurons of the neocortex. J. Neurophysiol. *54*, 782–806.

Mendoza, G., Peyrache, A., Gámez, J., Prado, L., Buzsáki, G., and Merchant, H. (2016). Recording extracellular neural activity in the behaving monkey using a semichronic and high-density electrode system. J. Neurophysiol. *116*, 563–574.

Millhouse, O.E., and DeOlmos, J. (1983). Neuronal configurations in lateral and basolateral amygdala. Neuroscience *10*, 1269–1300.

Mitchell, J.F., Sundberg, K.A., and Reynolds, J.H. (2007). Differential attention-dependent response modulation across cell classes in macaque visual area V4. Neuron *55*, 131–141.

Nelson, M.J., and Pouget, P. (2012). Physical model of coherent potentials measured with different electrode recording site sizes. J. Neurophysiol. *107*, 1291–1300.

Oemisch, M., Westendorff, S., Everling, S., and Womelsdorf, T. (2015). Interareal Spike-Train Correlations of Anterior Cingulate and Dorsal Prefrontal Cortex during Attention Shifts. J. Neurosci. *35*, 13076–13089.

Onorato, I., Neuenschwander, S., Hoy, J., Lima, B., Rocha, K.-S., Broggini, A.C., Uran, C., Spyropoulos, G., Klon-Lipok, J., Womelsdorf, T., et al. (2020). A Distinct Class of Bursting Neurons with Strong Gamma Synchronization and Stimulus Selectivity in Monkey V1. Neuron. bioRxiv. https://doi.org/10.1016/j.neuron.2019.09.039.

Pedemonte, M., Goldstein-Daruech, N., and Velluti, R.A. (2003). Temporal correlations between heart rate, medullary units and hippocampal theta rhythm in anesthetized, sleeping and awake guinea pigs. Auton. Neurosci. *107*, 99–104.

Pettersen, K.H., and Einevoll, G.T. (2008). Amplitude variability and extracellular low-pass filtering of neuronal spikes. Biophys. J. *94*, 784–802.

Peyrache, A., and Destexhe, A. (2019). Electrophysiological monitoring of inhibition in mammalian species, from rodents to humans. Neurobiol. Dis. *130*, 104500.

Peyrache, A., Dehghani, N., Eskandar, E.N., Madsen, J.R., Anderson, W.S., Donoghue, J.A., Hochberg, L.R., Halgren, E., Cash, S.S., and Destexhe, A. (2012). Spatiotemporal dynamics of neocortical excitation and inhibition during human sleep. Proc. Natl. Acad. Sci. USA *109*, 1731–1736.

Pham, D.T., Dimov, S.S., and Nguyen, C.D. (2005). Selection of K in K-means clustering, Published online January 1, 2005. https://journals.sagepub.com/doi/abs/10.1243/095440605X8298?cookieSet=1.

Rao, S.G., Williams, G.V., and Goldman-Rakic, P.S. (1999). Isodirectional tuning of adjacent interneurons and pyramidal cells during working memory: evidence for microcolumnar organization in PFC. J. Neurophysiol. *81*, 1903–1916.

Rutishauser, U., Schuman, E.M., and Mamelak, A.N. (2006). Online detection and sorting of extracellularly recorded action potentials in human medial temporal lobe recordings, *in vivo*. J. Neurosci. Methods *154*, 204–224.

Rutishauser, U., Schuman, E.M., and Mamelak, A.N. (2008). Activity of human hippocampal and amygdala neurons during retrieval of declarative memories. Proc. Natl. Acad. Sci. USA *105*, 329–334.

Rutishauser, U., Ross, I.B., Mamelak, A.N., and Schuman, E.M. (2010). Human memory strength is predicted by theta-frequency phase-locking of single neurons. Nature *464*, 903–907.

Rutishauser, U., Ye, S., Koroma, M., Tudusciuc, O., Ross, I.B., Chung, J.M., and Mamelak, A.N. (2015). Representation of retrieval confidence by single neurons in the human medial temporal lobe. Nat. Neurosci. *18*, 1041–1050.

Schomburg, E.W., Anastassiou, C.A., Buzsáki, G., and Koch, C. (2012). The spiking component of oscillatory extracellular potentials in the rat hippocampus. J. Neurosci. *32*, 11798–11811.

Senzai, Y., and Buzsáki, G. (2017). Physiological Properties and Behavioral Correlates of Hippocampal Granule Cells and Mossy Cells. Neuron *93*, 691–704.

Shinomoto, S., Shima, K., and Tanji, J. (2003). Differences in spiking patterns among cortical neurons. Neural Comput. *15*, 2823–2842.

Sirota, A., Montgomery, S., Fujisawa, S., Isomura, Y., Zugaro, M., and Buzsáki, G. (2008). Entrainment of neocortical neurons and gamma oscillations by the hippocampal theta rhythm. Neuron *60*, 683–697.

Soltesz, I., and Losonczy, A. (2018). CA1 pyramidal cell diversity enabling parallel information processing in the hippocampus. Nat. Neurosci. *21*, 484–493.

Spampanato, J., Polepalli, J., and Sah, P. (2011). Interneurons in the basolateral amygdala. Neuropharmacology *60*, 765–773.

Spruston, N. (2008). Pyramidal neurons: dendritic structure and synaptic integration. Nat. Rev. Neurosci. *9*, 206–221.

Srivastava, G., Crottaz-Herbette, S., Lau, K.M., Glover, G.H., and Menon, V. (2005). ICA-based procedures for removing ballistocardiogram artifacts from EEG data acquired in the MRI scanner. Neuroimage *24*, 50–60.

Staba, R.J., Wilson, C.L., Fried, I., and Engel, J., Jr. (2002). Single neuron burst firing in the human hippocampus during sleep. Hippocampus *12*, 724–734.

Stauffer, W.R., Lak, A., Yang, A., Borel, M., Paulsen, O., Boyden, E.S., and Schultz, W. (2016). Dopamine Neuron-Specific Optogenetic Stimulation in Rhesus Macaques. Cell *166*, 1564–1571.

Takahashi, K., Kim, S., Coleman, T.P., Brown, K.A., Suminski, A.J., Best, M.D., and Hatsopoulos, N.G. (2015). Large-scale spatiotemporal spike patterning consistent with wave propagation in motor cortex. Nat. Commun. *6*, 7169.

Tamura, H., Kaneko, H., Kawasaki, K., and Fujita, I. (2004). Presumed inhibitory neurons in the macaque inferior temporal cortex: visual response properties and functional interactions with adjacent neurons. J. Neurophysiol. *91*, 2782–2796.

Tasic, B., Yao, Z., Graybuck, L.T., Smith, K.A., Nguyen, T.N., Bertagnolli, D., Goldy, J., Garren, E., Economo, M.N., Viswanathan, S., et al. (2018). Shared and distinct transcriptomic cell types across neocortical areas. Nature *563*, 72–78.

Taxidis, J., Anastassiou, C.A., Diba, K., and Koch, C. (2015). Local Field Potentials Encode Place Cell Ensemble Activation during Hippocampal Sharp Wave Ripples. Neuron *87*, 590–604.

Terem, I., Ni, W.W., Goubran, M., Rahimi, M.S., Zaharchuk, G., Yeom, K.W., Moseley, M.E., Kurt, M., and Holdsworth, S.J. (2018). Revealing sub-voxel motions of brain tissue using phase-based amplified MRI (aMRI). Magn. Reson. Med. *80*, 2549–2559.

Tort, A.B.L., Brankačk, J., and Draguhn, A. (2018). Respiration-Entrained Brain Rhythms Are Global but Often Overlooked. Trends Neurosci. *41*, 186–197.

Trainito, C., von Nicolai, C., Miller, E.K., and Siegel, M. (2019). Extracellular Spike Waveform Dissociates Four Functionally Distinct Cell Classes in Primate Cortex. Curr. Biol. *29*, 2973–2982.e5.

van der Maaten, L., and Hinton, G. (2008). Visualizing Data using t-SNE. J. Mach. Learn. Res. *9*, 2579–2605.

Van Geit, W., Gevaert, M., Chindemi, G., Rössert, C., Courcol, J.-D., Muller, E.B., Schürmann, F., Segev, I., and Markram, H. (2016). BluePyOpt: Leveraging Open Source Software and Cloud Infrastructure to Optimise Model Parameters in Neuroscience. Front. Neuroinform. *10*, 17.

Vigneswaran, G., Kraskov, A., and Lemon, R.N. (2011). Large identified pyramidal cells in macaque motor and premotor cortex exhibit "thin spikes": implications for cell type classification. J. Neurosci. *31*, 14235–14242.

Viskontas, I.V., Ekstrom, A.D., Wilson, C.L., and Fried, I. (2007). Characterizing interneuron and pyramidal cells in the human medial temporal lobe *in vivo* using extracellular recordings. Hippocampus *17*, 49–57.

Washburn, M.S., and Moises, H.C. (1992). Electrophysiological and morphological properties of rat basolateral amygdaloid neurons *in vitro*. J. Neurosci. *12*, 4066–4079.

Wilson, F.A.W. (1994). Functional synergism between putative y-aminobutyrate-containing neurons and pyramidal neurons in prefrontal cortex. Proc. Natl. Acad. Sci. USA *91*, 4009–4013.

Yelnik, J., and Percheron, G. (1979). Subthalamic neurons in primates: a quantitative and comparative analysis. Neuroscience *4*, 1717–1743.

Zanos, S., Zanos, T.P., Marmarelis, V.Z., Ojemann, G.A., and Fetz, E.E. (2012). Relationships between spike-free local field potentials and spike timing in human temporal cortex. J. Neurophysiol. *107*, 1808–1821.

Zelano, C., Jiang, H., Zhou, G., Arora, N., Schuele, S., Rosenow, J., and Gottfried, J.A. (2016). Nasal Respiration Entrains Human Limbic Oscillations and Modulates Cognitive Function. J. Neurosci. *36*, 12448–12467.

STAR★METHODS

KEY RESOURCES TABLE

REAGENT or RESOURCE	SOURCE	IDENTIFIER
Software and Algorithms		
MATLAB 2017b	MathWorks	RRID: SCR_001622
Python	Python.org	RRID: SCR_008394
Neuron 7.5 Simulator	NEURON	RRID: SCR_005393
OSort cell sorting algorithm	Rutishauser et al., 2006	RRID: SCR_015869 https://rutishauserlab.org/osort/
Allen Institute Brain Modeling kit	Allen Institute for Brain Science	https://github.com/AllenInstitute/bmtk
Human cells for *in vitro* recordings	Allen Institute for Brain Science	https://celltypes.brain-map.org/
Blue Brain optimization (BluePyOpt)	Blue Brain Project	https://github.com/BlueBrain/eFEL
QRS Tool	Allen et al., 2007	https://jallen.faculty.arizona.edu/content/qrstool-and-cmetx-software-calculating-metrics-cardiac-variability
Dataset of human medial temporal lobe single neuron activity during declarative memory encoding and recognition	Faraut et al., 2018	https://datadryad.org/stash/dataset/doi:10.5061/dryad.46st5
Cardiac-motion EAP Cell Classifier	This manuscript	https://github.com/rutishauserlab/cellclassifier
Human all active models	This manuscript	https://github.com/AllenInstitute/Human_all_active_models_EAP
Other		
Neuralynx Neurophysiology System	Neuralynx	Cat# ATLAS 128
Spencer SEEG electrodes	Ad-Tech Medical	RD06R-SP05X-000
Behnke-Fried Hybrid electrodes	Ad-Tech Medical	BF08R-SP05X- WB09R-SP00X-0B6
Alpha Omega MicroGuide System	Alpha Omega	Cat# STR-000021
Alpha Omege Hybrid Microelectrodes	Alpha Omega	Cat#IS08RSP10X-0T1

LEAD CONTACT AND MATERIALS AVAILABILITY

Further information and requests for resources should be directed to and will be fulfilled by the Lead Contact, Ueli Rutishauser (ueli.rutishauser@cshs.org). The spike-time data from the in-vivo recordings in epilepsy patients, the EAP waveform classifiers, the *in vitro* recordings used to generate the single-neuron models, and the all active human single neuron models are available publicly for download (see Key Resources Table). This study did not generate new unique reagents.

EXPERIMENTAL MODEL AND SUBJECT DETAILS

A total of 31patients volunteered to participate in the *in vivo* experimental recordings (see Tables S1 and S2 for age and gender). All subjects gave informed consent and all protocols were approved by the Institutional Review Board of Cedars-Sinai Medical Center. Eleven patients were implanted with hybrid depth electrodes for monitoring the source of intractable epilepsy (for details, see Carlson et al., 2018; Rutishauser et al., 2010). In addition to these recordings, we recorded electrophysiological signals intraoperatively from 20 patients with motor disorders being implanted with deep brain stimulation (DBS) electrodes (for details, see Kamiński et al., 2018).

Model neurons were based on human neurons obtained from cortical tissue resected from 11 patients for the purpose of removing epileptogentic tissue (Table S3). Surgical specimens were obtained from local hospitals in collaboration with a network of neurosurgeons. All patients provided informed consent for tissue donation, and all experimental uses were approved by the respective hospital Institutional Review Board before commencing the study (for more details, see http://celltypes.brain-map.org/donors).

METHOD DETAILS

In vivo neural recordings with cardiac monitoring

Eleven patients were implanted with hybrid electrodes for monitoring the source of intractable epilepsy (for details, see Rutishauser et al., 2010). Each electrode contained a bundle of 8 microwires for recording single unit activity and local field potentials. Electrodes

targeted, bilaterally, the amygdala, hippocampus, anterior cingulate cortex, orbitofrontal cortex, and pre-supplementary motor area. The location of the electrodes was verified with post-operative T1-weighted structural MRI scans registered to an atlas in MNI152 space (Kamiński et al., 2017). Broadband (0.1 Hz to 9 kHz) electrophysiological signals were recorded postoperatively at a 32 kHz sampling rate using a 256-channel ATLAS system (Neuralynx, Bozeman MT). Signals were locally referenced to one of the eight microwires in the bundle.

In addition to these recordings, we recorded electrophysiological signals intraoperatively from 20 patients with motor disorders being implanted with DBS electrodes (for details, see Kamiński et al., 2018). During each intraoperative session, two microelectrodes were placed to map the transitions through different brain regions and to identify the target for the DBS electrode. Microelectrode recordings targeted the subthalamic nucleus, the substantia nigra, or the putamen. Target locations were determined stereotaxically based on preoperative 3T T1- and T2-weighted MRI scans co-registered with preoperative CT scans (Kamiński et al., 2018). Broadband (0.1 Hz to 32 kHz) electrophysiological signals were recorded intraoperatively at a 40 kHz sampling rate using a NeuroOmega system (Alpha Omega, Nazareth Il.). Signals were referenced to the cannula that delivered the microwire.

During neurophysiological recordings we simultaneously recorded the electrocardiogram (EKG) from two surface electrodes placed on the chest and referenced to the neck. EKG was sampled at 1 kHz and recorded and amplified through the headstages used to record LFP from the macro-contacts on the neurophysiological recording electrodes. EKG was filtered offline (3rd order FIR filter, 3-30 Hz bandpass) and the peak of the QRS wave was detected using the open-source software QRSTool (Allen et al., 2007). Interbeat intervals (IBIs) measured the time between subsequent R-waves in milliseconds.

All-active single-neuron models with motion simulation

In this paper, we constructed model neurons and simulated motion for 4 biophysically-realistic human cortical aspiny (AP) neurons and 10 spiny (SP) neurons obtained from cortical tissue resected from 11 patients for the purpose of removing epileptogentic tissue (Table S3). Each *in vitro* experiment resulted in a set of electrophysiology responses to standardized current injection protocols as well as a reconstructed morphology (both available online via https://celltypes.brain-map.org/).

Each human single-neuron model was generated based on a set of electrophysiological features (Figure 3). Moreover, since dendritic and somatic features of cell morphology affect various spatiotemporal characteristics of the EAP waveform, we accounted for the full dendritic reconstruction available for each neuron (Anastassiou et al., 2015; Gold et al., 2007, 2006; Holt and Koch, 1999; Jia et al., 2019; Pettersen and Einevoll, 2008). To capture the intricacies of the electrophysiological behavior of single-neurons and allow better convergence of the parameters, the model generation workflow was divided into three stages. At each stage, a new set of conductances (Na, K, and Ca dependent) were added to the reconstructed morphology and the relevant electrophysiological features were calculated from the experimental voltage traces using eFEL (https://github.com/BlueBrain/eFEL) - the conductance density for each conductance of a model is then fitted to replicate the experimental electrophysical features within a python based evolution algorithm toolbox BluePyOpt (Van Geit et al., 2016). This involves optimizing passive conductances along with capacitance, reversal potential and axial resistance in the initial stage with target features e.g., voltage deflection, steady state voltage being added to the multi-objective optimization program, followed by Ih conductances with features related to the voltage sag under hyperpolarizing current. Finally, the rest of the active conductances were added to the model to minimize errors between experimental and model spiking features such as action potential amplitude and width, interspike interval, spike adaptation index (see Figure 3 for illustration of optimization procedure).

After a single neuron model was optimized, we simulated the EAP using NEURON 7.5 simulator (https://www.neuron.yale.edu/neuron/) in combination with the Brain Modeling Toolkit (https://github.com/AllenInstitute/bmtk). This toolkit (Gratiy et al., 2018) is capable of simulating a variety of observables directly supported by NEURON (e.g., spikes, and membrane voltages), as well as plugging in modules for computing additional observations (e.g., the extracellular potential). The EAP traces were computed using the line-source approximation, which assumes that membrane current is uniformly distributed within individual computational compartments and that the medium is homogeneous and isotropic (Gratiy et al., 2018). The model was simulated at a sampling rate at 30kHz. The stimulation was a 23.44 ± 1.27 Hz Poisson-like synaptic input at 44 locations on the cell to elicit an average of 108+/- 52 SD spikes per model.

To account for the spatial extent of the recording electrode, we recorded the extracellular potential via the line-source approximation in a dense grid (1 μm spacing) consisting of 32 columns and 480 rows (total 14,400 recording channels). To faithfully account for the EAP waveform of an electrode spanning 32 × 32 μm^2, we simulated the EAP in every location of the discretized mesh within this surface area. The final EAP waveform for the location at the center of the recording surface area was the average from the EAP waveform mesh. To mimic cardiac motion, we used a similar approach. Specifically, we simulated cardiac motion as a sinusoidal movement among adjacent recording channels during a 1Hz cycle. Figure 4A and 4B illustrate examples of 3 μm motion, in which the movement was among 4 recording channels sites during each cycle. At each recording site we simulated a variety of motion amounts (from 1 to 20 μm) to identify which amount of motion best estimated the motion observed experimentally. We estimated the motion and recording distance in our *in vivo* recordings by comparing *in vivo* values to the model data. For each EAP from an *in vivo* recorded unit we calculated the AMP and identify the location around every model with the same EAP AMP. In Figure 4D, therefore, each circle is one distance estimate (n = 69 *in vivo* hippocampal neurons x 14 models = 966 distance estimates total).

It follows that each single-cell model is linked to different datasets: on the one hand, the *in vitro* electrophysiology and reconstructed morphology datasets used to generate the conductance-based models in the first place and, on the other hand,

the simulated EAP dataset, used to link a specific model to *in vivo* recorded units from human hippocampus. This link becomes particularly important as it allows EAP properties recorded from hippocampal units *in vivo* to be associated to morphological (aspiny versus spiny, Figure 5) and electrophysiological (Figures 6F–6H) *in vitro* properties of human single cells.

QUANTIFICATION AND STATISTICAL ANALYSIS

Spike detection and sorting of single units

The broadband signals from the *in vivo* recordings and the model neurons were filtered in the 300-3,000 Hz band using a zero-phase lag filter (four-pole Butterworth filter, see code release). The intracellular spiking activity of model neurons provided the spike times for the model EAP data. Spikes from *in vivo* recordings were detected and sorted using the semi-automated template-matching algorithm OSort (Rutishauser et al., 2006). We excluded channels with interictal epileptic activity. Each single unit was manually evaluated and verified based on a variety of features: (1) the spike waveform, (2) the percentage of interspike intervals (ISIs) less than 3 ms, (3) the ratio of the waveform extremum and the standard deviation of the noise, (4) the pairwise projection distance in the clustering space between all isolated neurons on the same microwire, (5) the coefficient of variation of the ISI and (6) the cluster isolation distance (Rutishauser et al., 2008). Of the 11 waveform features we used to cluster, three features (HW, TPW, and HW MC) were weakly but significantly correlated with isolation distance (R^2 = 0.02, 0.11. 0.11, p = 0.016, 0.016, 0.16 respectively). The NS, BS1, and BS2 cells all had similar isolation distance, signal-to-noise ratio, and inter-spike interval (Figures S7A–S7C).

We recorded a total of 1,090 well-isolated neurons: 183 in hippocampus, 256 in amygdala, 148 in anterior cingulate, 145 in orbitofrontal cortex, 278 in pre-supplementary motor area, 14 in putamen, 35 in subthalamic nucleus, and 32 in substantia nigra.

Single unit firing properties and coherence with LFPs

Mean firing rate was calculated as the inverse of the mean of the interspike intervals during the recording session. Coefficient of variation (CV) is a measure of spike train variability and has a value equal to 1 for a Poisson process. CV was calculated as the standard deviation of the interspike interval divided by mean of the interspike interval. The local variation (LV) is similar to CV but measures variation in adjacent ISIs and was calculated according to Shinomoto et al., 2003.

Some neurons appear to have rate modulations during the cardiac cycle because the electrode motion influences spike detection and spike sorting. To quantify the degree of spike rate modulation we constructed raster plots and PSTHs of each cell aligned to the heartbeat (Figures S8A and S8B). The window began 20 ms before the heartbeat and ended when the median of that session's interbeat interval had elapsed (median IBI, 804 ± 156 SD ms or 75 ± 15 beats per minute). We interpolated from 0 to 2π over this window to calculate the ''phase'' that each spike occurred relative to the heartbeat. The Rayleigh test of nonuniformity was applied to these spike-phases to determine if a cell's firing rate was significantly modulated during the heartbeat ($p < 0.01$). In addition, we calculated 1,000 bootstrapped values for each neuron by randomly jittering the hearbeat times by up to 5 s and recalculating the spike rate at these jittered times. A cell was said to be significantly modulated by the heartbeat if the Rayleigh test-statistic was greater than 99% of these shuffled data and had a p value less than 0.01. In addition to calculating rate changes we also designed a metric to ascertain how well-isolated the spike sorting was at different time points in the cardiac cycle. First, we performed PCA on the EAP waveforms and calculated the Euclidean distance between each spike waveform and all other spikes in principal component space (using the components that explained 95% of the variance). Then, for each spike at a given time point in the cardiac cycle, we identified the 10 spike waveforms that were closest to it in EAP -PCA space and asked how many of these spikes were inside the same unit cluster and how many were outside the cluster. A value of 0 indicates the cell is well-isolated from other waveforms, while a value of 100% indicates that all of the nearest waveforms are outside the unit cluster (Figure S8E). We show that changes in spike rate during the cardiac cycle are likely due to missed detection of spikes outside the cluster, either because these spikes are assigned to a different cluster or fall into the background noise (Figure S8).

For each neuron we also calculated the autocorrelation function. Each spike train was represented as a binary vector and the autocorrelation was calculated with 500 ms lag using the xcorr function in MATLAB (functions available from MATLAB, all custom scripts for calculating EAP features and classifiers available for download in code release). Values were normalized to the zero lag value and are reported as spike rates. Similar to reports in the rodent hippocampus (e.g., Barthó et al., 2004 and other reports in the human hippocampus, e.g., Viskontas et al., 2007) we observed that the autocorrelation function could be characterized as three types of responses: regular-spiking cells that had a late peak > 20 ms, bursty cells with low-latency peaks < 20 ms, and cells that had a uniform distribution with no clear peak (Figure 7B). To quantify these three types of responses we first measured the median of the autocorrelation function and calculated the residuals of the autocorrelation function at 3-150 ms lag. If the residuals in this time window were homoscedastic ($p > 0.05$ Engle's Arch test), the cell was identified as having a uniform autocorrelation with a rate equal to the median. If, however, the autocorrelation function failed the test of homoscedasticity then the maximum local peak in the autocorrelation function was detected. Cells with peaks that occurred at less than 20 ms were labeled as bursty cells, in line with other reports that cells in the human hippocampus burst with ISIs up to 20 ms in duration (Staba et al., 2002; illustrated as light shaded bars in Figure 7B). Because this metric does not account for the amount of time spent bursting, we also calculated an additional, stricter, burst metric: the summed magnitude in the 0-20 ms window of the time zero-scaled autocorrelogram, i.e., the probability that a spike

will be followed by other spikes at a burst ISI latency. For the subset of neurons with a peak < 20 ms we also report the percent where this metric is greater than 0.05 (i.e., bursts more than 5% of the time, Figure 7B dark shaded bars). All other cells with peaks > 20 ms were labeled as regular spiking.

To determine if hippocampal cells entrained to local oscillations, we analyzed the LFP on each microwire relative to the spike time of each neuron. Broadband signals were first locally referenced to one of the 8 microwires that did not contain spiking activity and then low-pass filtered for frequencies < 300 Hz using a zero-lag FIR filter and down sampled to 1 kHz. Because the waveform of the EAP is known to significantly contaminate low-frequencies of the LFP (Anastassiou et al., 2015) we never compared LFPs and units recorded on the same microwire. We only compared LFPs to single units on different wires in the same bundle.

For each cell-LFP pair we first extracted 500 ms of the LFP signal before and after each spike. We chose such long windows because we were interested in frequencies as low as 3 Hz. Averaging these segments gives the spike triggered average (STA). We then estimated the frequency spectrum of the STA and of each spike-LFP segment using multitaper analysis with a time-bandwidth product of 7 and 3 tapers resulting in a frequency resolution of 3.5 Hz (Chronux toolbox). Spike filed coherence was then calculated by dividing the frequency spectrum of the STA by of the average frequency spectrum around each spike (Fries et al., 2001). We calculated the SFC for each neuron-LFP pair and observed a strong peak in the spike field coherence in the theta frequency band (3-8 Hz, Figure 7D) that appeared to differ for different cell classes. We then filtered the LFP in several frequency bands (theta = 3-8 Hz, alpha = 8-12.5 Hz, beta = 12.5-30 Hz, low gamma = 30-50 Hz, and high gamma 50-90 Hz) and estimated the phase of the analytic signal at each spike time using the Hilbert transform. To determine if a neuron exhibited a significant phase preference we applied the Rayleigh test for non-uniformity ($p < 0.01$) and also compared our phase-concentration metrics bootstrap shuffled data (see next paragraph). To quantify how strongly a neuron's spikes were concentrated around a specific oscillatory phase, we estimated the kappa value of the Von Mises distribution (Circular Statistics Toolbox [Berens, 2009]). Kappa values range from 0 to 1 (though we have z-scored the values to shuffled data, see paragraph below). The reciprocal of Kappa is analogous to the variance of the normal distribution, i.e., higher kappa indicates a smaller variance in spike phase.

As previously noted, some cells appear to change their firing rate throughout the cardiac cycle because motion compromises spike sorting and detection (Figure S8). Since these rhythmic fluctuations in spike rate could potentially affect the SFC metric at low-frequencies near the heart rate (heart rate is about 1-2 Hz), we performed a necessary control: we compared all SFC and Kappa values to bootstrap shuffled data (Figure S9). For each neuron-LFP pair we extracted the LFP and spikes around each heartbeat. We then randomly mismatched these beat-locked LFP-traces with beat-locked spike trains. This shuffling procedure preserves beat-related changes in spikes and LFP but will disrupt any spike-LFP relationships that are not tied to the heart. We performed 200 bootstraps and recalculated the SFC and Kappa values. We then z-scored the SFC and Kappa data to these bootstrapped values to effectively subtract off any spurious cardiac-related spike-LFP relationships. For example, the neuron-LFP pair in Figure S9A has high spike-field coherence and Kappa values at low frequencies < 2 Hz due to the changes in firing rate and the LFP signal around the heartbeat due to electrode motion (Figure S9C). After z-scoring to shuffled data, this spurious coherence is removed without affecting underlying spike-field relationships (Figure S9D).

Statistical comparisons of spike and spike-LFP values were performed using nonparametric statistics, Kruskal-Wallis for multiple groups, Wilcoxon rank-sum for two groups ($p < 0.05$, corrected for multiple comparisons). Chi-square and Fishers-exact tests were used for comparisons of cell counts among groups and types of responses, e.g., comparing the number of BS1 and BS2 cells that synchronize to local theta.

Quantification of EAP waveform features

For each *in vivo* and model neuron we extracted from the high pass filtered 32 kHz signal, 32 samples (1 ms) before and 50 samples (1.56 ms) after the EAP extremum. We then upsampled this signal to 100 kHz and realigned all waveforms to the extremum.

We calculated four standard features of the average EAP waveform: extremum amplitude (AMP), half-width time (HW), trough-to-peak time (TPW), and repolarization time (REP) (Figure 1D). These EAP features are often used to delineate functional classes *in vivo* and in slice recordings (e.g., Anastassiou et al., 2015; Barthó et al., 2004; Ison et al., 2011; McCormick et al., 1985; Mitchell et al., 2007; Peyrache et al., 2012; Rutishauser et al., 2015; Trainito et al., 2019). AMP is the magnitude of the extremum of the EAP in microvolts. HW is the total time in milliseconds that the EAP trough dips below half the AMP value. TPW measures the time in milliseconds that elapses from the EAP trough to the EAP peak, the first local maximum after the trough. REP measures the amount of time required for the EAP to reach half of the peak value and is an estimate of the EAP repolarization time. In some brain regions, the EAP width features appeared to be bimodally distributed. To assess bimodality, we calculated the Hartigan's Dip Test of multimodality. In addition, we assessed whether a single Gaussian distribution or a mixture of two Gaussian distributions better fit the distributions (assessed by minimizing Aikake Information Criterion for Gaussian mixture models with 1 or 2 distributions).

In addition to these features of the mean EAP waveform, we measured how these features change throughout the duration of the cardiac cycle. For *in vivo* data we binned the spikes in 100 ms bins that began 20 ms before each heartbeat ended at the median interbeat interval duration (804 ± 156 SD ms). We then averaged the EAP waveform of all the spikes that occurred in each bin to provide an average EAP waveform at each time during the cardiac cycle. We used these binned EAPs to calculate features at each time

point in the cardiac cycle. For model data we calculated the average EAP at every location around the cell. We then selected a random location around the cell and sampled the average EAP sinusoidally from this fixed location to simulate cardiac motion (see model generation method).

For each average EAP during each cardiac bin, we calculated AMP, HW, TPW, and REP as above. Plotting these features against the phase of the cardiac cycle (as in Figure 1E) highlights how these features change as a function of cardiac motion. We divided each of these traces by their mean to give a percent change from mean. To quantify the strength of these changes we fit a cosine function to each trace using circular-linear regression. The amplitude of this cosine fit estimates the percent change in the feature during the cardiac cycle and is termed the Modulation Index (MI). For example, a value of 5 indicates that the feature increased up to 5% of its mean value throughout the duration of the cardiac cycle. AMP MI was said to be strongly modulated by the cardiac cycle if the amplitude of this sinusoidal fit was significantly different from zero ($p < 0.05$) and it was greater than 95% of bootstrap shuffled data. Bootstrapping was performed by shuffling the EAP waveforms associated with each spike time for 200 iterations.

In addition, we quantified the extent to which each width features covaried with AMP during the cardiac cycle using linear regression. We refer to the slope of this linear regression as the Motion Correlation (MC). A value of 0 indicates that the width feature did not vary with AMP. A value of −2 for TPW MC, for example indicates that TPW decreases by 2% for every 1% increase in AMP.

Identification of EAP waveform clusters using PCA and k-means clustering

To identify clusters of cell types in the experimental data, we performed principal component analysis on the normalized EAP features of the hippocampal neurons (Figure S2; Figures 2A and 2C). We only selected neurons with significant strongly modulated AMP MI for this analysis because we were interested in cells with EAP waveforms that were most affected by cardiac motion. We performed k-means clustering (k = 1-9 clusters, 1000 iterations with random starting locations) on the principal components that explained 90% of the variance of the EAP features (Figures S2A and S2B, 3 components in standard feature space, 7 components in standard + motion feature space). The optimal number of clusters was identified by minimizing the density function f(K) (Pham et al., 2005 as in Jia et al., 2019). f(K) is the ratio of the real distortion to the estimated distortion and has a value of 1 for uniformly distributed data. In the standard feature space (Figure 2A), f(k) is lowest for k = 2, indicating that 2 clusters is the optimal number of clusters. In addition to k-means clustering we performed hierarchical clustering with Ward linkage and present dendrograms (Figure 2E). Both approaches yield highly overlapping results. When only using standard features, we identified two cell classes, one with narrow spike (NS) and one with broad spike waveforms (BS). With the addition of motion features, BS cells clustered into two separate groups labeled BS1 and BS2. Clusters are shown with t-distributed stochastic neighbor embedding (tSNE) for visualization purposes only (van der Maaten and Hinton, 2008).

We used a similar PCA-kmeans approach to identify SP1 and SP2 model neuron types. First, we randomly selected 25 EAPs from different sites around each of the SP model neurons. We then applied PCA specifically to the motion features (MI and MC) of the SP waveforms and performed k-means clustering to identify 2 groups of EAPs: SP1 and SP2. These groups differed in multiple features, e.g., SP2 has more negative HW MC and TPW MC than SP1 (Figure 6B). We then tabulated the number of EAPs of each model that were assigned to either the SP1 or SP2 EAP cluster. A model neuron was labeled SP1 (or SP2) if the majority of its EAPs (> 13/25 EAPs) belonged to the SP1 (or SP2) cell cluster.

SVM Classification of EAPS

We trained several linear SVM classifiers to discriminate between different types of experimental EAPs (NS versus BS, BS1 versus BS2) and EAPs derived from model neurons (AP versus SP, SP1 versus SP2). For experimental-based classifiers, we trained and tested using random subsets of the experimentally-recorded EAPs and used the labels NS, BS1, and BS2 derived from the k-means clusters in Figure 2C. For the model-based classifiers, we randomly selected 25 EAPs with AMP 40 ± 20 microvolts (the distribution of EAP AMPs recorded *in vivo*). We then trained on the EAPs from a subset of models and tested on the EAPs from the remaining models. The model neurons were constructed from *in vitro* patch clamp recordings of human neurons and the AP and SP labels were determined by the morphological reconstructions of these neurons and their associated spines (see also section above on model generation). The SP1 and SP2 labels were derived from the EAP-feature k-means clustering described in the preceding section.

In all cases, each reported classifier is a "bootstrap composite" of 1,000 individual SVM classifiers each trained and tested on a different subset of EAPs to ensure robustness and generality to new data. The result of each composite classifier therefore gives both a classification label and a percent indicating the fraction of individual bootstrapped classifiers that assigned the same label. For example, the Standard Experiment-based Classifier (Figure 5A), assigned the neuron in Figure 1E middle panel the label BS with 99% agreement (i.e., 99% of the individual classifiers in this composite classifier gave the label BS). For each application of a classifier, labels were assigned based on more than 50% agreement of the individual classifiers, though most cells had much higher values (mean agreement = 96% ± 10% for the Standard Experiment-Based classifier in Figure 5A). Confusion matrices and accuracy bar-plots show the performance on left out data (e.g., Figure 5A). The SVM Beta coefficients estimate the contribution of each feature to the SVM plane that divides the classification space with higher values indicating a larger contribution to the classification model (e.g., Figure 5B).

The primary motivation for constructing classifiers was to cross-validate the experimental and model-based results. We applied experimental-based classifiers to model EAPs to identify model neurons in the experimental space (NS or BS, BS1 or BS2) (Figures 5C and 6F right). Similarly, we applied model-based classifiers to the experimental EAPs to identify experimental neurons in the model space (AP or SP, SP1 or SP2; Figures 5F and 6F left).

DATA CODE AND AVAILABILITY

Code for calculating EAP features and classifying cell types was custom-written in MATLAB and is available on GitHub (https://github.com/rutishauserlab/cellclassifier). The all-active human single-neuron models were constructed in Python and are also available on GitHub (https://github.com/AllenInstitute/Human_all_active_models_EAP).